DOI: 10.1002/ (aenm.201800611)
Article type: Full Paper

In Situ Analysis of Solvent and Additive Effects on Film Morphology Evolution in Spin-Cast Small-Molecule and Polymer Photovoltaic Materials

Eric F. Manley, Joseph Strzalka, Thomas J. Fauvell, Tobin J. Marks, Lin X. Chen**

E. F. Manley, T. J. Fauvell, Prof. T. J. Marks, Prof. L. X. Chen
Department of Chemistry and the Argonne-Northwestern Solar Energy Research (ANSER) Center, Northwestern University, 2145 Sheridan Road, Evanston, Illinois 60208, USA
E. F. Manley, T. J. Fauvell, Prof. L. X. Chen
Chemical Sciences and Engineering Division, Argonne National Laboratory, 9700 South Cass Avenue, Lemont, Illinois, 60439, USA
J. Strzalka
X-ray Science Division, Argonne National Laboratory, Lemont, Illinois 60439, USA
E-mail: (t-marks@northwestern.edu, l-chen@northwestern.edu)

Keywords: in situ GIWAXS, spin-coating, additive, polymer, organic solar cells

Solvent and processing additives have dramatic effects on the morphology and photovoltaic response of spin-coated organic solar cell (OSC) active layers. Traditionally, film morphology analyses were carried out after completion of the spin-coating/drying process, leaving critical temporal/morphological aspects of film maturation unknown. Here, to elucidate such details of film morphology/order evolution during spin-coating, solvent and additive effects are systematically investigated for three representative, diverse OSC active layer materials using combined *in situ* grazing incidence wide angle x-ray scattering (GIWAXS) and optical reflectance. Two archetypical semiconducting donor (p-type) polymers, **P3HT** (poly(3-hexylthiophene)), and **PTB7** (poly[[4,8-bis[(2-ethylhexyl)oxy]-benzo[1,2-b:4,5-b']dithiophene-2,6-diyl][3-fluoro-2-[(2-ethylhexyl)-carbonyl]-thieno[3,4-b]thiophenediyl]]), and semiconducting donor small-molecule, **p-DTS(FBTTh2)2** (7,7'-(4,4-bis(2-ethylhexyl)-4H-silolo[3,2-b:4,5-b'] dithiophene-2,6-diyl)bis(6-fluoro-4-(5'-hexyl-[2,2'-bithiophen]-5yl)-benzo[c][1,2,5]thiadiazole) systems are studied using chloroform (CF), chlorobenzene (CB), and 1,2-dichlorobenzene (DCB) as neat solvents and with processing additives 1-chloronapthalene (CN), diphenyl ether (DPE), 1,8-diiodooctane (DIO), and 1,6-diiodohexane

(DIH). *In situ* GIWAXS identifies several key trends: 1) for neat solvents, rapid crystallization occurs that risks kinetically locking the material into multiple crystal structures or crystalline orientations; and 2) for solvent + additive processed films, morphology evolution involves sequential transformations on timescales ranging from seconds to hours. Divergence between polymer and small molecule film evolutions depends on the additive/semiconductor molecular interactions. In films processed with CN or DPE, where π-planes dominate the additive/semiconductor interactions, both polymers and small molecules follow similar evolutions, completing in the initial 1-5 min. When processed with DIO or DIH, in which side chains dominate the additive/semiconductor interactions, polymer film maturation times are up to 9 h. In contrast, initial crystallization times < 10 s are observed for small molecule films, followed by periods of increased x-ray scattering isotropy and thickness reduction. Additionally, unlike polymer films, the small molecules exhibit additive-dependent crystal structures. This *in situ* GIWAXS information on OSC donor intermediate morphologies, evolution timescales, and divergent evolutions should help inform spin-coating studies and ultimately guide OSC manufacture.

1. Introduction

The past decade has witnessed dramatic advances in the performance of solution-processed organic solar cell (OSC)[1–5] and organic thin film transistor (OTFT)[6–8] materials. Consistent OSC power conversion efficiencies (PCEs) over 11 %[9–11], with some reaching > 13 %,[12] and OTFT mobilities > 1 ($cm^2V^{-1}s^{-1}$) [8] indicate the realistic possibility of new soft matter technologies. Note that these high-performance laboratory devices are often produced via spin-coating, a reliable fabrication process that enables rapid prototyping and basic research. However, the transition to high throughput film fabrication processes such as blade-coating, roll-to-roll printing, and others will require understanding of film morphology-forming mechanisms operative in spin-coating processes that optimize organic device performance.[13] Traditionally, optimizing device performance relied on empirical screening of spin-casting

parameters such as solvent, processing additive, and spin-speed, followed by post-processing analysis of which morphologies are produced by which coating conditions.[14–16] For OSC film morphology, grazing incidence wide-angle x-ray scattering (GIWAXS) is especially powerful for monitoring crystallinity, orientation, donor-acceptor intermixing,[14–18] and developing an *ex post facto* understanding basis for otherwise completely empirical "recipes." While informative, post-deposition analysis can miss important temporal characteristics of film growth -- processes which can only be identified by *in situ* techniques. *In situ* film growth studies utilizing GIWAXS and other techniques during film deposition and drying have been employed by several groups, including our own, to understand crystalline morphology development in organic electronic thin films.[19,20] Characterizing morphology during the film formation process can elucidate important mechanistic pathways and inform rational solution processing parameter optimization.

Several recent studies have reported *in situ* optical and x-ray analyses of organic film growth by roll-to-roll printing,[21] blade coating,[13,22–26] and slot die casting,[27,28] as well as static substrate methods such as drop casting.[29],[30–32] However, the very high mechanical stability required for *in situ* GIWAXS during spin-coating presents a particular instrumental challenge which was only recently surmounted. We recently reported on the temporal characteristics of **PTB7** (poly[[4,8-bis[(2-ethylhexyl)oxy]benzo[1,2-b:4,5-b']dithiophene-2,6-diyl][3-fluoro-2-[(2-ethylhexyl)-carbonyl]-thieno[3,4-b]thiophenediyl]]) spin-coating using the high-throughput *in situ* GIWAXS system at the Advanced Photon Source (APS) Beamline 8-ID-E.[20] This work contributed to the small body of *in situ* GIWAXS analyses of organic film spin-coating, to our knowledge consisting only of the seminal work of Amassian,[33–37] and more recently, Wu.[38]

Previous *in situ* GIWAXS work[20] focused on how solvents and processing additives influence **PTB7** film morphology evolution, with **PTB7** selected as an archetypical high-performance OSC polymer and accepted design paradigm for OSC polymers. That study

identified a diverse range of temporal phenomena, with single solvent systems having morphological transformation times < 3 s and those of additive-containing films ranging from min to >1.5 h for 1,8-diiodooctane (DIO). Interestingly, the formation times inversely track the solvent additive boiling points (b.p.) with DIO lowest at 168 ºC versus CN and DPE with b.p.'s of ~260 ºC. Estimating the additive-**PTB7** intermolecular interactions with Hansen solubility parameters[39] argues that interactions between the long solubilizing polymer alkyl substituents and DIO molecules are significant and explain the unexpectedly long film maturation times. In contrast, CN and DPE likely interact with the polymer π-system, which may be less accessible due to the solution phase self-aggregation of **PTB7**.[40] These results contrast the commonly held orthodoxy that b.p. should dominate such temporal effects and argue that simple Hansen solubility factors can rationalize additive - polymer backbone/side-chain interactions, hence film morphology evolution.

This contribution assesses the generality of the above observations by extending the *in situ* analysis to other additives and OSC donors. Using *in situ* GIWAXS and optical reflectance measurements during spin-coating, we carefully examine how materials optimization variables, e.g., solvent and additive choices, impact the film morphology evolution of three extensively used neat OSC materials, two polymers and one small-molecule: poly(3-hexylthiophene) (**P3HT**),[41] **PTB7**,[42] and high performance small-molecule, **p-DTS(FBTTh$_2$)$_2$** (7,7′-(4,4-bis(2-ethylhexyl)-4H-silolo[3,2-b:4,5-b′]dithiophene-2,6-diyl)bis-(6-fluoro-4-(5′-hexyl-[2,2′-bithiophen]-5yl)-enzo[c][1,2,5]thiadiazole); abbreviated as **DTS**)[43] (**Figure 1**). **P3HT** is a relatively crystalline[41,44,45] homopolymer in thin films and offers an instructive contrast to the more amorphous[42,46] charge transfer co-polymer **PTB7**. Their responses to film processing solvent/additive conditions should help assess processing-morphology generalities for OSC polymers. Polymeric OSC materials have long been known to form lamellar crystal structures.[47,48] However, while this description is qualitatively correct, depending on the polymer and processing, crystalline characteristics can vary. These include variations in

crystalline orientation on the substrate, overall crystallinity, and side-chain (100) and π-π stacking (010) d-spacings.[16,49,50] Thus, developing *in situ* understanding of how these factors impact polymer design should be particularly informative. In contrast, small-molecule **DTS** probes differences that arise when adjusting processing conditions for polymers versus small molecules. Unlike polymeric counterparts, small-molecule materials may readily form different crystal structures.[51–55] Simple changes in molecular structure [52–54] or processing solvent[55] can dramatically affect crystal packing. Additionally, the present **DTS** results can be compared/contrasted with previous *in situ* studies under different processing conditions.[33,35,36] All three of the present subject materials deliver high OSC performance and have stimulated research upon which the present *in situ* results can build.

Utilizing the aforementioned APS *in situ* GIWAXS instrumentation,[20,56] an expanded solvent + additive parameter space is examined, totaling over 50 *in situ* characterization sets and representing a substantially larger dataset than in previous studies.[33–38] The evolution of both lamellar (100) and π-π stacking (010) reflections is analyzed along with simultaneously acquired film thickness data. Thin films deposited from neat chloroform (CF, b.p. 61 ºC), chlorobenzene (CB, b.p.131 ºC), o-dichlorobenzene (DCB, b.p. 180 ºC) are characterized, as well as CF and CB mixed with 1% and 3% v/v 1-chloronapthalene (CN, b.p. 263 ºC), diphenyl ether (DPE, b.p. 258 ºC), 1,8-diiodooctane (DIO, b.p. 168 ºC), and 1,6-diiodohexane (DIH, b.p. 141 ºC). In total, 19 solvent + additive combinations are used for each of the three donor systems to provide a detailed evaluation of solvent/additive molecular structure effects on film formation dynamics, with important insights into the interplay of solute/solvent-additive structures in directing specific film morphologies. It will be seen that key distinctions are revealed between additive-driven crystallization in small-molecule **DTS** films and those of the polymeric materials, with divergent crystal structures in addition to distinct morphology formation timescales evident in additive-processed **DTS** films. More subtle distinctions exist between the homo-polymer **P3HT** and charge transfer co-polymer **PTB7** film formation, with

insights provided into polymer pre-spin-coating aggregation states -- free-chain vs self-folded in solution effects on crystallization and access to different crystalline orientations. This detailed evaluation offers guidelines for solvent and additive choice based on desired morphological outcome, as well as definitive time-evolution information to enhance device fabrication reproducibility. The information should inform future device optimization and rationally steer film morphology to specific desired characteristics for optimum performance.

2. Results

2.1 Contents of the Following Sections. Here we present an extensive data analysis including a very large number of *in situ* GIWAXS measurements. Thus, for the reader's benefit we briefly preview the contents. In **Section 2.2** the optical absorption characteristics of all materials and solvent combinations are briefly discussed. Section **2.3** provides a glossary of the key terminologies used to describe the *in situ* GIWAXS results. *In situ* GIWAXS and film thickness data are reported in **Sections 2.4-2.5**, with **Section 2.4** focusing on morphology evolution for all three semiconductors processed from additive-free CF, CB and DCB. **Sections 2.5.1** (**P3HT**), **2.5.2** (**PTB7**), and **2.5.3** (**DTS**) discuss the *in situ* GIWAXS and thickness results for each semiconductor processed from additive-containing CF and CB solutions. Morphological evolution times are then summarized in **Section 2.6** for all three semiconductors under all processing conditions. **Section 2.7** presents a Hansen solubility parameter molecular interaction analysis, examining the dominant interactions between additives and semiconductors. Following the Results, the Discussion is partitioned into three main topics. First, **Section 3.1** addresses the formation of single-solvent processed films, including kinetically locked morphologies resulting in multiple crystal structures. **Section 3.2** discusses solvent additive influence on morphology evolution, including the differing impact of additives primarily interacting with π-planes versus those primarily interacting with alkyl chains. **Section 3.3** provides guidelines for solvent and additive selection for desired morphological consequences. Finally, **Section 4** presents Conclusions.

2.2. Optical absorption characteristics of single-solvent and additive-containing solutions. The optical absorption spectra of the three semiconductors in dilute solutions were measured in all solvent/additive combinations and are presented in the Supporting Information (SI) **Figure S1**. When dissolved in a single-solvent, all three materials show the same trend with a slight blue-shift in going from DCB to CB to CF. Solution in solvent + additive mixtures exhibit only negligible deviation from those dissolved only in CF or CB.

2.3. Describing morphology evolution in organic thin films. We begin with the terminology used in the following GIWAXS discussion.

1. *Morphology Formation Time*. Time required for crystallite formation and thickness evolution completion. Once full morphology is attained, no significant additional changes are observed.

2. *Crystallization Times (Onset, Completion)*. Temporal features of crystalline scattering observable by GIWAXS. Onset is defined as the time point when scattering features are first detected, while completion is defined as the time when the scattering peaks are stable in height (within 5% of the final peak height) and peak position, with no significant further changes.

3. *Solvent Thinning Transition Time (t_{thin}).* Time point at which sample thickness has completed the rapid thinning that occurs during spin-coating. This rapid fall in thickness is then followed by a more gradual thickness decline under some processing conditions.

4. *Thickness Evolution Completion Time (t_{finish}).* Time point when film thickness is stable and no longer contracting, i.e., when thickness reaches within 1% of the final value.

5. *Lamellar Stacking (100) Peaks*.[15,16] X-ray scattering features assignable to periodicity in the lateral polymer backbone-to-backbone separation largely dictated by the side chain length. These are associated with a feature at q = 0.2 – 0.4 $Å^{-1}$. In-plane (q_{xy}) lamellar scattering arises from periodicity in the π-face-on molecular stacking normal to the substrate

plane, while out-of-plane (q_z) lamellar stacking scattering arises from periodicity in edge-on molecular orientation relative to the substrate plane.

6. *π-π Stacking (010) Scattering*.[15,16] X-ray scattering features assignable to periodicity between semiconductor π planes. Due to polymer backbone twists, and the insulating nature of alkyl side chains, molecular π-π interactions are crucial elements of charge transport in organic semiconductors.[14,57–59] Note that π-π stacking is usually assigned to a feature at q = 1.4 – 1.8 $Å^{-1}$. Out-of-plane (q_z) π-π stacking scattering is indicative of π-face-on molecular orientation relative to the substrate plane, while in-plane (q_{xy}) π-π stacking scattering features indicate edge-on molecular orientation relative to the substrate plane.

2.4. Additive-free, single-solvent P3HT, DTS, and **PTB7 film morphology evolution.** **Figure 2** shows the crystalline evolution of all three materials in additive-free CF solutions through representative line cuts and post-processing 2D images. For similar data for CB and DCB solutions see SI **Figures S2-1 and S2-2**. When spin-coated from additive-free solutions both **P3HT** and **DTS** exhibit the same sharp, rapid transition previously observed in single solvent **PTB7** films.[20] Abrupt onset of crystallinity occurs with negligible subsequent changes. The previous **PTB7** experiments[20] are reproduced and provided alongside the new **P3HT** and **DTS** data for close comparison. In **Figure 3**, which shows the morphology evolution for films spun from solutions of the aforementioned three solvents. The top row shows rapid crystallization with abrupt rise in lamellar scattering, and the bottom row shows optical reflectance-derived film thickness evolution. It is clear that crystallite formation occurs concurrent with the solvent thinning transition. Resulting time points for solvent thinning transitions (t_{thin}), crystallization onsets, and crystallization completion are summarized in **Table 1.** As observed previously for **PTB7**,[20] t_{thin}, and the crystallization onset/completion times increase with solvent boiling point.

In marked contrast to the **PTB7** results where the abrupt transitions yield the same final π face-on morphology in all single-solvent processed films, **P3HT** and **DTS** morphology

evolution is more complex. **P3HT** displays a mix of both face-on and edge-on crystallite orientations while **DTS** concludes with two different edge-on structures. These **DTS** morphologies were previously characterized by Abdelsamie, et al.[33], however with CB they did not detect the lower q scattering peak, indicating a second structure, without prolonged film drying. Note that the relative ratios of the two film states in both **P3HT** and **DTS** are very sensitive to experimental conditions. These film samples were prepared and measured multiple times, revealing differing relative ratios of the two crystalline phases, although crystallization is invariably abrupt and rapid (see SI, **Figures S3-1** and **S3-2**). These results imply that these rapid single-solvent transitions trap the material in a kinetically directed morphology. Because the solution to film transitions for **P3HT** and **DTS** have multiple possible crystalline phases, small batch-to-batch variations in concentration and temperature can afford differing ratios of phases.

2.5 Films processed from solvent/additive mixtures.

2.5.1. P3HT film morphology evolution in solvent/additive mixtures. The effects of the different processing additives on **P3HT** film morphology evolution are summarized in **Figure** and **5**. Figure 4 shows representative line cuts and post processing 2D images for films spun from 3% v/v additive in CB. Similar data for CF solutions and 1% v/v additive solutions are in the SI **Section S8**. Figure 5 summarizes evolution data for all additive-processed **P3HT** films including evolution of the lamellar (100) and π-π stacking (010) peaks as well as film thickness. These data presented in Figure 5D show that t_{thin} remains dependent on the solvent, with $t_{thin} \approx$ 1 - 2s for all films processed in CF and $t_{thin} \approx 6 – 7$s in CB regardless of the additive used. The film thickness has an initial rapid reduction followed by a gradual decline that extends over longer times. The t_{thin} and thickness evolution completion data are summarized in **Table 2**.

Evident in Figures 4 and 5 is that **P3HT** exhibits multiple distinct crystalline evolution patterns and timescales. All films exhibit growth of a single out-of-plane scattering peak before transitioning to clearly edge-on crystallite orientation with multiple out-of-plane lamellar

reflections and an in-plane π-π stacking peak. These crystallization processes span a broad range of timescales, with some completing during the 60s spin-coating process, while others require extended drying periods to complete crystallization. Note that all additive-processed **P3HT** films have a final edge-on crystalline orientation with none exhibiting face-on orientation features observed in some films processed without additives. Thus, it is clear that the edge-on crystalline orientation is thermodynamically preferred for **P3HT** films. Films processed with DPE in CB and CF exhibit initial crystalline growth concurrent with rapid solvent thinning, followed by a period of steady, then oscillatory peak growth before finally reaching stable morphology. The timings of t_{thin}, t_{finish}, crystallization onset, oscillatory peak growth, and completion of crystallite formation are summarized in Table 2.

P3HT films processed with CN evolve on a similar timescale to those processed with DPE, however there are marked differences in the evolution. Rather than consistently initiating with the solvent thinning transition, initial crystalline peak formation for 3% v/v CN processed films occurs at 24.2 s (3% v/v CN in CB), and 55.4 s (3% v/v CN in CF). In CB, the lamellar scattering peak grows steadily until a point at which time the out-of-plane scattering intensity declines as the crystallites lose preferential orientation and become more isotropic, evident in the 2D scattering images (SI **S16**). In CF, there is steady peak evolution over a slower timescale, but without the high intermediate maximum. Coincident with this peak growth is a peak shift evident in Figure 5B for all the films. The timings of t_{thin}, t_{finish}, crystallization onset, start time for the secondary crystalline evolution phase and the completion of crystallite formation are summarized in Table 2.

When processed with DIO, **P3HT** evolution proceeds through a dramatically longer film formation process than with CN and DPE. Similar to DPE-processed films an initial peak in the q_z direction is observed at $q_z \approx 0.39$ Å^{-1} on solvent thinning. While this initial peak is evident at early times, no higher order lamellar or (010) π-π reflections are visible until later when slow onset of lamellar and π-π stacking reflections begins with completion of the edge-on

morphology. The t_{thin}, t_{finish}, intermediate crystallization onset and finish, and the primary crystallization start and completion data are summarized in Table 2. With CF + 3% v/v DIO processed films, the onset of this secondary growth process is not complete, even over a 5 h data acquisition period so it is assumed that the morphology evolution times are > 18,000 s. In films processed with DIH, there is a progression similar to that for the DIO films, however, the time period is shorter. Upon thinning, the initial intermediate peak at $q_z \approx 0.38$ Å^{-1} initiates, followed by a time of negligible growth, similar to that seen for DIO, until secondary growth begins and the slower (100) peak formation is completed. The t_{thin}, t_{finish} values, intermediate onset and finish, and primary crystallization completion points are shown in Table 2. Peak position shifting occurs over this time with the start/end at: $q_z = 0.380$ Å^{-1} / 0.398 Å^{-1} (1% v/v in CF), $q_z = 0.385$ Å^{-1} / 0.395 Å^{-1} (3% v/v in CF), $q_z = 0.394$ Å^{-1} / 0.40 Å^{-1} (1% v/v in CF), and $q_z = 0.376$ Å^{-1} / 0.395 Å^{-1} (3% v/v in CB). See **Table S12-2** for all lamellar peak d-spacings in these additive processed P3HT films. Here the (010) π-π stacking growth (Figure 5C) occurs concurrent with primary lamellar crystalline growth. Thus, in films with intermediate scattering as in DIO/DIH-processed films, (010) π-π stacking growth begins only after the intermediate phase of lamellar peak growth. The resulting d-spacings for the π-π stacking interactions are summarized in Table S12-2.

To summarize, all additive-processed **P3HT** films yield the same edge-on crystalline orientation, in contrast to **P3HT** films processed in neat solvents. However, CN and DPE-processed films exhibit faster morphology evolution than DIH and DIO-processed films. All CN-processed films attain final morphology in less than 170 s and all DPE-processed films in less than 330 s. In contrast, DIH-processed films attain final morphology on timescales as long as 2600 s, and DIO-processed films require > 18000 s in the longest case. Notably, even in films with very slow morphology evolution, an initial GIWAXS polymer scattering peak is always visible. This contrasts with **PTB7** films where slow morphology evolutions include a significant period with negligible polymer x-ray scattering.

2.5.2. PTB7 film morphology evolution in solvent/additive mixtures. Figure 6 and **Figure 7** show the evolution of **PTB7** films processed with DIO, DIH, DPE, and CN in CF and CB. The CB + DIO, CN and DPE data are new results reproducing previous work.[20] This confirms the divergent film maturation pathways identified previously, although there are minor differences in timescale attributable to slight differences in temperature and concentration. Figure 6 shows representative line cuts and post-processing 2D images of films spun from 3% v/v additive in CB. Similar data for CF solutions and 1% v/v additive solutions are available in SI **S9**. Figure 7 summarizes evolution data for all additive-processed **PTB7** films including fitted peak evolution for the lamellar (100) and π-π stacking (010) peaks as well as thickness evolution. π-π stacking evolution is shown as the change in the position of the out-of-plane (q_z) scattering feature as there is an overlap between the face-on π-π stacking peak ($q_z \approx 1.6$-1.65 Å^{-1}) and the solvent scattering profile ($q_z \approx 1.4$-1.7 Å^{-1} depending on additive) in all four solvents. It is thus difficult to differentiate the rise in π-π stacking growth from already present solvent scattering, while observing the timing of the peak shift from solvent scattering to π-π stacking scattering offers a more unambiguous metric. The reflectance data in Figure 7C show that t_{thin} continues to depend on the principal solvent, with $t_{thin} \approx 0.8$ - 1 s for all CF films and $t_{thin} \approx 6.5$ – 8.5 s for CB films. The initial fall in thickness is followed by an extended gradual decline. The t_{thin} and thickness evolution data for all films are shown in **Table 3**.

The GIWAXS results show that in CN-processed **PTB7** films the lamellar stacking crystallization onset occurs for most films coincident with thinning, although the 3% v/v CN in CB processed films exhibit delayed onset similar to that in the other semiconductors. The onset is followed by a period of steady peak growth, extending up to 175 s until crystallization is complete. The timings for t_{thin}, t_{finish}, and crystallization onset/completion are presented in Table 3. Due to synchrotron time constraints, the 1% v/v CN in CB film was not re-examined, and the data here are from the previous report,[20] which, however, did not include the full lamellar stacking (100) analysis discussed here.

In the DPE-processed films, after a thinning transition coincident crystallization onset, steady, although slightly oscillatory peak growth is observed which finishes in ~335s. The timings for t_{thin}, t_{finish}, and crystallization onset/completion are summarized in Table 3**Error! Reference source not found.**. Interestingly, crystallization seems to be complete well before thickness evolution is complete in all four DPE-processed films. As with the CN-processed films, because of synchrotron time constraints, the 1% v/v DPE in CB processed film was not re-examined and the results presented here are from the previous report[20] but with more comprehensive analysis. As noted previously,[20] **PTB7** films processed with DIO form at orders of magnitude slower rates than with CN or DPE. After thinning, there are no polymer diffraction peaks. An initial isotropic peak is then observed at $q \approx 1.5$ Å^{-1} following the solvent thinning transition, and with a significant delay, the beginning of lamellar and π-π stacking scattering is observed and steadily increases until film formation is complete. The lamellar scattering crystallization onset is significantly delayed from the solvent thinning transition, followed by a steady peak growth over ca. 6600 s. Timings for t_{thin}, t_{finish}, and crystallization onset/completion are shown in Table 3. The π-π stacking growth is most evident in the peak position shift from additive scattering to final π-face-on peak position. Previous studies using 17keV x-rays identified the isotropic feature at $q \approx 1.5$ Å^{-1} of uncertain origin, but the present studies using higher energy 30 keV x-rays in the solution scattering experiment unambiguously assign this feature to DIO scattering at $q = 1.48$ Å^{-1}(see SI **Figure S5**). Note that films from CF as primary solvent evolve significantly more slowly, with 3% v/v DIO in CF requiring 9 h for full crystallization, likely reflecting the increased CF + additive film thicknesses **(**Figure 7C).

Finally, DIH-processed films again have formation characteristics similar to their DIO counterparts but with a reduced timescale. Following the thinning transition, there is an initial period with negligible polymer scattering followed by a delayed onset of crystallization and a steady rise in lamellar scattering over ca. 2500 s. The timings for t_{thin}, t_{finish}, and crystallization onset/completion are summarized in Table 3. The pure DIH solution scattering profile was

confirmed including the DIH scattering peak at q = 1.50 $Å^{-1}$ by an identical solution experiment with DIO (see SI). For all the additive-processed **PTB7** films, shifts in out-of-plane scattering as the peak transitions from additive scattering to polymer π-π stacking (Figure 7B) are concurrent with the lamellar rise. D-spacings for the lamellar and π-π stacking interactions for all additive processed films are provided in **Table S12-3**.

In summary, additive-processed **PTB7** films exhibit morphology evolution over dramatically divergent timescales. CN and DPE-processed films are complete in < 500 s in all solvent/additive combinations. Conversely, DIH and DIO-processed films are significantly slower, with the former requiring up to 4600 s and the latter up to 33000 s in the longest cases. Note that all films evolve to the same π face-on crystalline orientation.

2.5.3. Small-molecule DTS film morphology evolution in solvent/additive mixtures.

The temporal characteristics of **DTS** film morphologies processed from CF and CB with additives DIO, DIH, DPE, and CN additives are shown in **Figures 8** and **9**. In marked contrast to the above polymer films where morphology evolution pathways and timescales but not the final packing structures, are influenced by additives, the **DTS** final crystal structures are diverse and strongly influenced by the additives. The crystallization time scales are all relatively short with none requiring the times of DIO-processed polymer films. Figure 8 shows representative line cuts and post processing 2D images for films spun from 3% v/v additive in CB. Similar data for CF solutions and 1% v/v additive solutions are available in the SI. Figure 9 summarizes morphology evolution data for all additive-processed **DTS** films including fitted peak evolution for the lamellar (100) and π-π stacking (010) peaks as well as for thickness evolution. The data in Figure 9D show that t_{thin} again depends on the principal solvent, with t_{thin} ≈ 0.8-1.4 s for all films processed from CF and t_{thin} ≈ 4.5 – 5.6 s for those from CB. The final post-processing 2D scattering images are shown on the right for films from CB as principal solvent. The t_{thin} and thickness evolution data are summarized in **Table 4**.

The *in situ* small-molecule **DTS** scattering results indicate that films processed with CN have morphology formation timing similar to that of their polymer counterparts with an onset of crystallization independent of the solvent thinning transition at 3% v/v additive concentration, followed by a steady rise of the crystallization in 12.9 – 54.1 s, then by slight peak height decreases before complete crystallization (see Table 4 data). The resulting DTS films are highly crystalline as evident in the 2D scattering images (Figure 8 top right). Additionally, in a departure from the polymer CN processed films, the **DTS** films not only exhibit slight peak shifts after the initial intensity rise, but as the film crystallizes, the line cuts show that the single lamellar interaction peak evolves into two overlapping, but distinct reflections at q_z = 0.289 $Å^{-1}$ and q_z = 0.303 $Å^{-1}$ (d = 21.7 Å, d = 20.7 Å) towards the end of the crystallization process, revealing the added complexity of the highly crystalline film structure. The π-π stacking distance remains constant for 1% and 3% v/v CN in CB films: q_{xy} = 1.734 $Å^{-1}$and 1.728 $Å^{-1}$ (d = 3.623 Å, d = 3.636 Å) and = 1.698 $Å^{-1}$and 1.689 $Å^{-1}$ (d = 3.70 Å, d = 3.72 Å) for 1% and 3% v/v CN in CF films respectively. Full d-spacing data for all additive-processed **DTS** films are summarized in **Table S12-4**.

When **DTS** films are processed with DPE, there is a rapid, initial peak rise coincident with the solvent thinning transition, followed by a period of slower growth as well as a fall in peak intensity in films processed from CB as primary solvent. A rapid shift in peak position occurs at the end of crystallite formation rather than gradually over the entire crystallization process. Finally, full morphology is complete on a similar timescale to that of the polymeric films processed with DPE (see Table 4 for t_{thin}, t_{finish}, and crystallization onset/completion data). Note also, as evident in Figure 8, the resulting crystal structure when processed with DPE is markedly different from that under any other processing condition. Thus, the side chain interactions are at q_z = 0.262 – 0.267 $Å^{-1}$ with a secondary reflection at q_z = 0.484 - 0.509 $Å^{-1}$ corresponding to a d-spacing of 23.5 – 24.0 Å. The π-π stacking interaction is at q_{xy} = 1.34 $Å^{-1}$, corresponding to a d-spacing of 4.7 Å. These d-spacings are significantly larger than in films processed with any

other additive or without additives, indicating that DPE has a particularly unique interaction with this small molecule. This alternate crystalline structure is consistently apparent in 1% and 3% v/v mixtures with both CF and CB. In comparison, for **DTS** films processed with DIO, initial crystallization occurs very rapidly, starting at the thinning transition, and quickly reaching completion. All the films go through a significant GIWAXS peak position shift during the rise, starting at a higher q_z value and then shifting towards the final peak location at q_z = 0.290 – 0.293 $Å^{-1}$.

Interestingly, in contrast to all other additive/molecule combinations where additive effects are more dramatic at greater additive concentrations, the DIO-processed **DTS** films appear to exhibit the greatest peak shifts and extended crystallization times for the 1% v/v DIO rather than for the 3% v/v/ DIO films. This likely reflects the particular nature of this structural evolution as DIO directs from the kinetic morphology indicated by a higher q_z peak to the thermodynamically preferred morphology with a lower q_z peak; in higher concentrations, the thermodynamically preferred morphology is present in greater abundance at an earlier time. Thus, with greater DIO concentrations, the peak shift begins at a point closer to the lower q_z peak and completes on a faster time scale. Similar *in situ* behavior was reported by Abdelsamie *et al* in a study of **DTS** films processed from 0.4% v/v DIO in CB.[33] To confirm this result, a 0.4% v/v DIO in CB-processed film was examined here and yielded essentially identical results (SI **S4**). Interestingly, after the initial peak rise, there is a slower component as the out-of-plane scattering peak height slowly declines and becomes more isotropic. This relaxation is very slow, but more rapid than the time required for full crystallization in the DIO-processed polymer films discussed above (see SI for extended evolution process plots). Finally, completion of thickness evolution is slow with final structure realization instrumentally limited. Thus, even though crystallite evolution is complete over a short time scale, the additive remains in the films for extended times, similar to the polymeric films. Timings for t_{thin}, t_{finish}, primary crystallization onset/completion, and completion of all morphological changes are compiled in Table 4. DIH-

processed **DTS** films behave similarly to those processed with DIO. There is rapid initial crystallization coincident with the thinning transition that quickly reaches initial completion. A peak position shift occurs in the lamellar ordering peak as it shifts from higher q_z to the final q_z = 0.286 – 0.290 $Å^{-1}$ position (Figure 7B). Additionally, there is gradual relaxation in out-of-plane peak intensity as the peak shifts to a more isotropic state before the crystallization process is finally complete and an extended thickness evolution is observed. Timings for t_{thin}, t_{finish}, primary crystallization onset/completion, and crystallization completion are presented in Table 4. The π-π stacking growth (Figure 9C) is clearly concurrent with the primary lamellar crystalline growth in the CN, DIO, and DIH-processed films. In DPE films, due to the significant deviation in crystal structure from the other films, the relatively weak π-π stacking feature is at q_{xy} = 1.34 $Å^{-1}$ with significant overlap with the DPE scattering feature. Thus, the rise of the π-π interaction is difficult to detect, however, completion is evident when lamellar evolution is complete.

In summary, solvent additive-processed small-molecule **DTS** films exhibit significant distinctions from their polymeric counterparts. First, crystallite formation occurs on a far more rapid timescale, especially with DIO and DIH-processed films. For DIO-processed films, the primary crystallite growth is complete within 14 s in the longest example, orders of magnitude shorter than in polymer films, however further thickness reductions and slight changes in crystallinity extend over a far longer timescale. Similarly, in DIH-processed **DTS** films, primary crystallite formation occurs within < 10 s for all films, however the total morphology evolution including thickness reduction and changes in scattering peak intensity extend over a far longer time. In all CN-processed films, crystallite formation is complete within 58 s, with the total morphology evolution complete within 100 s, and in DPE- processed films, crystallite evolution extends up to 292 s while total morphology evolution is complete by 340 s. It is of note that in CN and DPE processed films, the morphology evolution timescales are of a similar order of magnitude to similarly processed polymer films. The second major distinction versus

additive-processed polymer films is that the different additives have dramatically different impacts on the resulting crystal structures. Notably, DPE-processed **DTS** affords a completely different crystal structure than under any other processing conditions. CN-processed films are notably more crystalline than all others with many off-axis scattering features in the 2D images. DIO and DIH-processed films have very similar crystalline structures.

2.6. Morphology Formation Time Scale Summary. The evolution characteristics for all single-solvent and CB + additive-processed films are summarized in **Figure 10** (CF + additive-processed films are summarized in the SI). The data are sorted by additive to display trends across molecules for the different additive systems. Apparent in the top panel of Figure 10 is the consistency of evolutions in single-solvent, additive-free films. In the lower panels, across all additives, the relative additive independence of the solvent thinning transition is clear. The extended evolution times of DIO and DIH-processed films for both polymers yields dramatically longer time axes. Additionally, while the primary crystallization of **DTS**:DIO/DIH films occurs on a much faster timescale than the polymers, the isotropic relaxation time is significantly extended, and final thickness evolution occurs on a similar order of magnitude as the extended polymer crystallite formation times.

2.7. Hansen Solubility Parameter Considerations. Hansen solubility parameters are a pragmatic means to illuminate favorable and unfavorable solubility interactions between molecules and macromolecules during spin-casting. Using the dispersion (δ_D), polar (δ_P), and hydrogen bonding (δ_H) Hansen parameters and eq. 1,[39] interaction radii (R_a) can be calculated. R_a provides insight into the strength of intermolecular interactions, between a solvent and solute with a smaller R_a indicating a stronger interaction.[39] Hansen parameters for the present materials were approximated using the Van Krevlen group contribution

$$R_a = \sqrt{4(\delta_{D2} - \delta_{D1})^2 + (\delta_{P2} - \delta_{P1})^2 + (\delta_{H2} - \delta_{H1})^2} \qquad (1)$$

method[60] as modified by Richter et al.[61] and Barton[62] for the calculations.[63] The use of the Barton terms is an addition from our previous study.[20] Approximate computed Hansen parameters for **PTB7**, **P3HT,** and **DTS** are given in the SI. Previous work showed that it is informative to include Hansen approximations of the side chains,[20] so the solubility parameters for the **PTB7** ethylhexyloxy (EHO) and the **P3HT** and **DTS** *n*-hexyl side chains were also estimated. Experimental or calculated DIO, CN, and DPE Hansen parameters are from the literature,[39,63,64] and DIH was treated using the same method as for DIO.[63] The interaction radii (R_a) for all additives and semiconductors were then calculated (see SI **S7**) and are compiled in **Table 5**.

Note from Table 5 that **P3HT** has a strong affinity for all the present additives. Furthermore, the side chain approximation reveals an additive affinity ordering, DIO > DIH > DPE/CN. Also, the **DTS** parameters indicate a clear difference between DPE and the other additives, tracking well with the divergent **DTS** crystalline morphology in DPE-processed films. Finally, **PTB7** once again shows a preference for CN/DPE in the full polymer calculation that switches to a preference for DIO/DIH the side chain approximation. Interestingly, for both polymers, the side chain approximation affords the best correlation with the observed film formation rates. Similarly, the slightly lower preference on switching from DIO to DIH tracks the faster formation times observed on changing the additive from DIO to DIH.

3. Discussion

The *in situ* x-ray scattering characterizations presented here provide new insight into the use of solvents + additives in fabricating organic thin-film electronics. The observed patterns in single-solvent additive-assisted film growth underscore the importance of understanding/-predicting additive-molecule interactions in film morphology evolution.

3.1. Rapidly formed, kinetically locked morphologies in single-solvent processed films. On spin-coating, additive-free solutions exhibit rapid crystallization coincident with the solvent thinning transition, similar to that previously observed for **PTB7** films.[20] However, in contrast

to **PTB7**, **P3HT** films yield a combination of crystalline orientations while **DTS** yields a mixture of crystal structures. Because of the rapid crystallization in single-solvent systems, both face-on and edge-on orientations[15] are observed in **P3HT** films. It appears that the edge-on crystalline orientation is thermodynamically preferred, as evidenced by the additive processed **P3HT** films (Figure 4). In those films the longer evolution times and extended opportunity to sample the morphological energy landscape eventually yields exclusive edge-on orientations. Thus, mixed orientations in the single-solvent systems can be attributed to some fraction of **P3HT** chains adopting a kinetically locked, metastable π face-on orientation reflecting the rapid solvent evaporation. A similar effect is observed for single-solvent **DTS** films with the two primary crystal structures (both edge-on) for **DTS** differing in side chain interaction distances. The higher q_z (d-spacing ≈ 13.7 Å) crystallites are only derived from the single-solvent systems, while the lower q_z crystalline orientation (d-spacing ≈ 20.7 Å) is observed in some of the additive-processed films. These structures were previously characterized by Abdelsamie[33] who assigned the higher q to a liquid crystalline phase and the lower q to a crystalline phase, however for the present purposes they will simply be identified with a more kinetically-driven and more thermodynamically-preferred phases. Interestingly, Abdelsamie does not report both phases in single-solvent CB film depositions, in accord with the present observations that the ratios between the kinetic and thermodynamically associated phases for both **P3HT** and **DTS** films exhibit variations for different beam times (SI S3). Thus, the rapid crystallization that affords the kinetically-trapped dual crystalline orientation is influenced by slight variations in solvent concentration, temperature, and sample handling that inevitably occur from experiment to experiment. This limited control over crystalline morphology in the rapidly evolving additive-free systems is generally underappreciated in assessing device morphology optimization and reproducibility, and likely a factor in understanding the importance of processing additives, thermal annealing, and solvent annealing to enhance OSC performance and performance reproducibility.[2,65,66] However, note that this dual morphology effect was not

observed in the **PTB7** films analyzed previously[20] and that observation is reproduced here. Such films all exhibit rapid evolution to exclusive π-face-on orientation, the same morphological orientation observed in additive-processed films, albeit on a different time-scale and with different relative final crystallinities. It appears that **PTB7** has only one feasible crystalline orientation, so the difference between ending in a kinetically-driven or thermodynamically-preferred state is less than for more morphologically labile **P3HT** and **DTS**. Thus, characterization of the multiple potential crystalline variations may be warranted when utilizing a single solvent that exhibits rapid thinning transition-mediated crystallization as in CF, CB, and DCB. In a system such as **PTB7** where there is only a single crystalline form, solvent choice can be made based on other considerations such as solubility, film thickness, and ease of processing. However, with materials such as **P3HT** or **DTS**, assessing the device performance of less controllable morphologies must take into account multiple crystalline orientations.

3.2. Morphology evolution determined by solvent additives. In films processed from solutions with additives, interesting similarities and variations in film morphology evolution are observed among the three semiconductor systems. The results reveal a marked distinction between the film morphology evolution characteristics for the small molecule and the two polymers. In all the combinations of additives and solvents, **DTS** invariably exhibits more rapid crystallization. However, the relative differences in crystallization rate differ between the different additive-processed films. As shown in Figure 10, the crystallization times for CN and DPE processed **DTS** films are shorter than their polymer counterparts, but are on a similar order of magnitude. This must reflect the greater mobility of the **DTS** molecules which can more easily organize into periodic structures than macromolecular chains.[48,67]

Nevertheless, any differences arising from distinctions between ordered aggregation in small molecule and polymer films should be consistent regardless of the specific additive used in processing. In contrast to the DPE and CN processed films, the crystallization times for DIO

and DPE processed **DTS** films are multiple orders of magnitude faster than for **P3HT** and **PTB7** films. This is far beyond the difference that one would expect based simply on faster ordering in small molecules than in polymers as it differs dramatically from the magnitude of formation time differences observed in all other aspects of this study. Note that fast crystallization occurs even when the DIO and DIH have not fully evaporated as indicated by the extended timescale required for full thickness evolution (Figure 9, Table 4). The DIO and DIH are not exiting the film significantly more rapidly than in the polymer films, yet the **DTS** primary crystallization is much faster than the polymers. Interestingly, for **DTS** films, the additive processed crystallization times follow the expected order based on additive b.p. where in DIH- and DIO-processed **DTS** crystallization occurs more rapidly than for CN and DPE-processed films. Only in the polymer films do the lower b.p. DIO- and DIH-processed films have significantly longer crystallization times. Thus, only in DIO- and DIH-processed films where the additive-material interactions involve side chains, does the small-molecule to polymer change have a large impact on the crystallization rate. However, in the CN- and DPE-processed films, where the interaction likely involves the molecular π-planes, the additive-material interaction effects on morphology evolution remain consistent for the small-molecule and polymers.

Beyond simple differences in morphology evolution time scales, the diverse **DTS** film crystalline morphologies also depend on the specific processing additive. When processed with CN, highly crystalline films result with a noticeable coexistence of two distinct side chain interactions having similar d-spacings. DIO and DIH yield similar scattering patterns reproducing the crystal structure described as the "crystal phase".[33] While there are clear distinctions between the scattering patterns in films processed from CN and DIO/DIH, most notably the appearance of multiple off-axis scattering peaks in CN-processed films, these can be largely attributed to the greater overall crystallinity in CN-processed films rather than changes in the unit cell. Similarly, in the CN-processed films, the divergence of the single side chain peak into two marginally distinct scattering features at longer times may result from larger

crystallites allowing greater diffraction resolution. However, for DPE-processed films, there is a completely new scattering pattern indicating a distinct crystal structure absent in the other additive-processed films or in any of the single-solvent-derived films. There is insufficient diffraction to fully characterize the unit cell, however it is notable that d-spacings of d ≈ 23.7 Å for the q_z side chain peak and d ≈ 4.7 Å for the very weak π-π stacking peak are larger than in other **DTS** films. Thus, DPE directs the molecule away from forming the structure preferred in films processed with other additives.

For **P3HT** and **PTB7**, similar overall interactions are observed with the different additives, although there are also some significant differences. **P3HT** consistently completes morphology formation on a shorter timescale than **PTB7** when processed with any of the additives. However, like **PTB7**, **P3HT** film morphology transformations when processed with DIO and DIH are dramatically slower than when processed with CN and DPE. In DIO- and DIH-processed films, **PTB7** transits a period of minimal polymer scattering before slow crystallization begins. In contrast for **P3HT** films, the initial out-of-plane scattering is present coincident with the solvent thinning transition and persists until the principal crystallization occurs much later in the film drying process. Both differences in morphology evolution rates and appearance of the initial scattering peak likely result from differences between the polymer solution structures. **PTB7** is heavily self-aggregated in solution,[40] as evidenced by vibronic structure in the optical absorption profile, while **P3HT** has an absorption profile without vibronic features in all solvent and additive mixtures examined, which is characteristic of free chains with conformational disorder[68–70] in solution. Previously we explored the possibility that some DIO intercalates into **PTB7** solution-phase aggregates due to the preferred side chain interactions.[20] In contrast, while the **P3HT** side chains should conceivably have similar interactions with DIO, the lack of a self-aggregating solution phase means that there may be some initial interaction between the **P3HT** side chains upon solvent thinning as evidenced by the initial **P3HT** scattering peak even if the remaining additive inhibits extended periodic network formation. It would also be

expected that DIH, with similar molecular interaction parameters would act similarly although on a slightly faster time scale since the Hansen interaction strength with the side chains is weaker. This agrees with the experimental results since DIH seems to invariably mimic DIO morphology evolution, but more rapidly.

Finally, while in previous **PTB7** work[20] no major distinctions between morphology evolution in films processed with CN and DPE were observed, by expanding the semiconductor set, key distinctions are identified. Notably, the total crystallization time for 3% v/v CN in CB-processed films goes through a significant five-fold increase from **DTS** to **P3HT** to **PTB7**, while the difference between **PTB7** and **DTS** is only two-fold in DPE. Additionally, there is a distinction between when crystallization initiates in CN versus DPE-processed films. In DPE, it is consistently coincident with the solvent thinning transition while in CN crystallization initiation is often slower with increasing additive concentration slowing the rate further. In CB, 3% CN films consistently initiate at ~25 s while in CF, it is more semiconductor dependent, with **DTS** and **PTB7** beginning near the thinning transition (3.5 s and 1.3 s, respectively) while **P3HT** initiates at ~55.4 s, near the end of spinning. The CN and DPE results imply slight but real molecular structure related interaction differences between the additive and the polymer π-planes. The more expansive and rigid CN π-plane likely engages in different π-interactions than more conformationally mobile DPE.

3.3. Guidelines for solvent/additive selection. Overall, the present analysis of solvent and additive effects across three distinct semiconducting materials yields design guidelines for preliminary assessment of solvent and additive effects on film morphology. Using a single solvent typically induces rapid morphology evolution, coincident with the solvent thinning transition, and affording kinetically-controlled crystallization. In molecular systems where multiple crystallite structures and/or orientations are possible, a mixture of these crystal phases is likely to evolve in the kinetically-controlled formation process. It may be possible to influence the resulting crystalline morphology using substrate modification or post processing

steps such as thermal/solvent annealing, however, those will likely be system-specific. Beyond the effects on crystallite formation, these choices will impact the resulting film thickness and overall film quality, which may significantly influence device performance.

When processing with added CN, it can be anticipated that highly crystalline materials will undergo complete crystallization within minutes of initiating spin-coating. None of the materials examined here undergo crystallization in greater than 3 min, but it is expected that higher CN concentrations may increase the time. DPE processed films operate on a similar timescale, with evolution complete within minutes of initiating spin-coating. However, rather than leading to increased crystallinity across all systems, DPE instead promotes an extended time where the primary crystallization is complete but film is still swelled with additive, allowing more subtle morphological changes. During this time, which we refer to as a period of morphological lability, there can be changes in crystal packing and crystalline orientation without extensive changes in overall crystallinity. This morphological lability time during drying could conceivably be used to achieve additional phase intermixing in bulk-heterojunction films. Additionally, note that in DPE-processed **DTS** films, a crystal structure forms that is distinct from those in films from the other processing conditions. Despite having similar morphological formation times, this crystalline structure distinction is not detected in the other polymer films and may be unique to the **DTS** + DPE combination.

In films processed with DIO and DIH, divergent morphology formation properties are observed for small molecules and polymers. In the polymer films, very long crystallization times are the norm, reaching well into hour long timescales for DIO while they are slightly more rapid in DIH but still extend well beyond the end of spin-coating. For small molecule **DTS**, rapid initial crystallization occurs followed by a period of morphological lability where the crystallites become more isotropic; however, this labile period is complete within min of the end of spin-coating, unlike the polymeric counterparts. Nevertheless, it is safe to assume that principal crystallization is complete during the 60s spin-coating process in DIO/DIH-

processed **DTS** films. Despite the differences in crystallization, note that residual additive will swell the film over an extended time scale in both small molecule and polymer films so care must be made to ensure dry films to avoid the negative impacts of residual DIO[71,72] (which likely apply to DIH as well).

Note that the observed additive effects are challenging to recreate in single-solvent films. The extended morphological lability period available in DPE, DIO and DIH processed films (much longer for DIO/DIH) likely underlies the optimal BHJ morphologies that it enables, since greater phase intermixing is possible during this time. The increased crystallinity afforded by CN processing coincides with the increased crystallization times in these films. While attempts to recreate these effects in slow drying single-solvent systems are worth exploring, the fast transition even in high b.p. DCB-processed films indicates that approach may be challenging. Care will be needed to design fabrication processes that recreate the extended formation effects of these additives, or materials must be chosen/discovered which afford high performance in kinetically-driven morphologies easily achieved in single-solvent processing.

The guidelines above present rational approaches to achieving desired outcomes in the crystalline properties of organic solar cell materials. To achieve a desired performance gain, these guidelines must then be paired with the appropriate understanding of the relationship between crystalline morphology and device performance in the specific material examined. There are extensive analyses available in the literature for correlating crystalline morphology characteristics with electronic device performance for **P3HT**,[73–78] **PTB7**,[20,42,46,79–82] **DTS**,[33,83–87] and many other materials.[8,14,57,58,88–91] These can serve as a combined resource with the work presented here for the purposes of rationally selecting thin film fabrication conditions towards an intended performance outcome.

Finally, we reiterate from our previous report[20] that the results reported here underscore the need for OSC fabrication reporting procedures to indicate the time between spin-coating and the following fabrication steps to permit fully reproducible results in additive-processed

films. Spin-coating is typically followed by a morphology locking annealing and/or vacuum deposition steps in device fabrication, and in cases such as active layer polymer solutions with DIH and DIO, it is possible that subsequent fabrication steps are unknowingly carried out during a period of film morphological lability where crystallization is incomplete.

4. Conclusions

Using *in situ* GIWAXS and optical reflectivity, the film formation dynamics during solution phase spin-coating and drying of three model OSC semiconductors, crystalline homopolymer **P3HT**, semi-crystalline push-pull polymer **PTB7**, and crystalline small molecule **DTS** are investigated with a broad series of solvent and processing additive combinations. Single solvent processed films spun from CF, CB, and DCB solutions exhibit consistent morphology evolution timing with crystallization tied to the solvent thinning transition. The evolution is kinetically driven and results in a mixture of crystalline orientations for **P3HT** and a mixture of crystal structures for **DTS**. In films processed with additives, divergent patterns of crystallization across the polymer/small molecule series are observed depending on the primary nature of the additive-material molecular interaction. In CN- and DPE-processed films where the additive-material interactions are strongest with the π-planes, consistent morphology formation times are observed with all materials completing crystallization and thickness evolution on a range of 0.5 - 5 min depending on additive concentration. In DIO- and DIH-processed films, where the primary additive-material molecular interactions occur at the side chains, vastly different crystallization times are observed between the polymer and small molecule films even as the timing for thickness evolution remains similar. DIO- and DIH-processed polymer films have crystallizations occurring on time scales ranging from 10 min - 9 h whereas DIO and DIH processed small molecule films all have primary crystallizations that finish in < 15 s, followed by a period of orientation shifting over an extended time. Furthermore, **DTS** exhibits additive dependent crystal structures, whereas all additive processed polymer films evolved into the same thermodynamically preferred orientation.

Broadly, this investigation represents an expansive and detailed data set and underscores the ability to analyze and process extensive *in situ* GIWAXS results during spin-coating. The results presented here should serve as a valuable resource during the rational design process of new materials/devices and can also serve as a guide for the desired properties when transitioning from spin-coating to higher throughput manufacturing processes.

5. Experimental Section

Polymer/Small Molecule Materials and Solvents. **P3HT**, **PTB7** and **p-DTS(FTTP)$_2$** were purchased from ONE-Material Inc. and used as received. Molecular weight (M_n) and polydispersity (PDI) were determined using high temperature GPC in trichlorobenzene, yielding M_n =21.3 kd; PDI = 2.75 for **P3HT** and M_n = 49.7 kd; PDI = 3.1 for **PTB7**. CF (Anhydrous ≥ 99% with 0.5-1% EtOH as stabilizer), CB (Anhydrous ≥ 99.8%), DCB (Anhydrous ≥99%), DPE (selectophore ≥ 99.9%), and DIO (98% with Cu stabilizer) were purchased from Sigma-Aldrich, and CN (≥ 97%) from TCI; all were used without further purification. All solvents were stored in an Ar atmosphere glove box. Solutions were mixed in the Ar glove-box and stirred overnight at 65 °C.

Spin-Casting. Films were spin-cast by depositing 50µl of 10 mg/mL polymer/small molecule solution onto bare, cleaned (sonicated in methanol, acetone, and isopropyl alcohol for 20 min each), Si substrates and then spinning at 1000 rpm (with an acceleration of 20 r/s^2) for 60 s and then allowing them to stand for the remainder of the data acquisition period. The depositions were carried out in a He-purged chamber. A sensor confirmed that the O_2 level was <1% for all depositions and subsequent data collection.

In Situ Spin-Coating GIWAXS Data Collection. Grazing incidence wide angle x-ray scattering (GIWAXS) data were collected at beamline 8-ID-E of the Advanced Photon Source (APS).[56] To provide high-quality data with high temporal and spatial resolution, the x-ray beam was focused to < 10 µm vertically at the sample by a Be compound refractive lens and then attenuated by 50% to reduce sample damage. Multiple timing protocols were used for

acquisition times ranging from 10 min to 9hrs. Acquisition time points were confirmed with the log files to account for any unintended computer delays that could adjust the intended acquisition timing. The start of timing is always defined as the point when spinning begins. Fully processed data for each film analyzed by *in situ* GIWAXS are provided in the SI, while the pertinent information for the differing crystallization kinetics are shown in Figures 5, 7, and 9. A diagram of the experimental setup as well as an analysis of the time onset of x-ray beam damage is provided in the SI of ref. 20.[20]

In Situ Spin-Coating Optical Reflectance Data Collection. Simultaneous with the GIWAXS experiments, visible reflectance data were taken with a Filmetrics F20 instrument at 200 ms intervals (some longer depositions used 1-2 s intervals and are labeled as such) to assess film thickness. All thicknesses were determined using the Filmetrics software package and a fast Fourier transform (FFT) model during the periods before the thinning transition when the thickness is dominated by solvent, and the refractive index (n) and extinction coefficients (k) were calculated from the reflectance data after the system had transitioned to thin film form. Timings were set using the integration time in the Filmetrics software, however there was an uncontrollable computer delay creating slight inaccuracies in those numbers. Thus, the timing between each acquisition was determined using the start and end of spinning which had known time points (0 and 60 s respectively) and assuming equal acquisition timing of the data between those two timings. This was done for each acquisition to ensure that any changes in computer delay between samples would be accounted for.

UV-Vis Absorption Measurements. UV-vis absorption measurements were taken with a Shimadzu UV-3600 spectrometer using quartz cuvettes to contain the polymer/small molecule solutions in all solvent/additive combinations. All solutions were 0.1 mg/mL in concentrations, and 1 mg/mL stock solutions were prepared in CF/CB/DCB and stirred overnight before 100 µl was transferred to vials containing the appropriate solvent/additive mixture concentrations, and then stirred overnight. Data are presented in the SI.

SI

Supporting Information is available from the Wiley Online Library or from the author.

Acknowledgements

E.F.M, T.J.F, L.X.C. and T.J.M acknowledge financial support from Argonne-Northwestern Solar Energy Research (ANSER) Center, an Energy Frontier Research Center funded by the U.S. Department of Energy, Office of Science, Office of Basic Energy Sciences under Award Number DE-SC0001059, by the U.S. Department of Energy, Office of Science, and Office of Basic Energy Sciences under Award Number DE-FG02-08ER46536. E.F.M. was also supported by Qatar NPRP grant 7-286-1-046. Solution scattering was performed at the DuPont-Northwestern-Dow Collaborative Access Team (DND-CAT) located at Sector 5 of the Advanced Photon Source (APS). DND-CAT is supported by Northwestern University, E.I. DuPont de Nemours & Co., and The Dow Chemical Company. Solution scattering data were collected using an instrument funded by the National Science Foundation under Award Number 0960140. Use of the Advanced Photon Source, an Office of Science User Facility operated for the U.S. Department of Energy (DOE) Office of Science by Argonne National Laboratory, was supported by the U.S. DOE under Contract No. DE-AC02-06CH11357.

Received: ((will be filled in by the editorial staff))
Revised: ((will be filled in by the editorial staff))
Published online: ((will be filled in by the editorial staff))

References

[1] W. Chen, Q. Zhang, *J. Mater. Chem. C* **2017**, *5*, 1275.

[2] L. Lu, T. Zheng, Q. Wu, A. M. Schneider, D. Zhao, L. Yu, *Chem. Rev.* **2015**, *115*, 12666.

[3] K. M. Pelzer, S. B. Darling, *Mol. Syst. Des. Eng.* **2016**, *1*, 10.

[4] S. B. Darling, F. You, *RSC Adv.* **2013**, *3*, 17633.

[5] K. A. Mazzio, C. K. Luscombe, *Chem. Soc. Rev.* **2014**, *44*, 78.

[6] B. Kumar, B. K. Kaushik, Y. S. Negi, *Polym. Rev.* **2014**, *54*, 33.

[7] A. Marrocchi, A. Facchetti, D. Lanari, C. Petrucci, L. Vaccaro, *Energy Environ. Sci.* **2016**, *9*, 763.

[8] H. Sirringhaus, *Adv. Mater.* **2014**, *26*, 1319.

[9] S. Li, L. Ye, W. Zhao, S. Zhang, S. Mukherjee, H. Ade, J. Hou, *Adv. Mater.* **2016**, *28*, 9423.

[10] D. Deng, Y. Zhang, J. Zhang, Z. Wang, L. Zhu, J. Fang, B. Xia, Z. Wang, K. Lu, W. Ma, Z. Wei, *Nat. Commun.* **2016**, *7*, 13740.

[11] W. Zhao, D. Qian, S. Zhang, S. Li, O. Inganäs, F. Gao, J. Hou, *Adv. Mater.* **2016**, 4734.

[12] W. Zhao, S. Li, H. Yao, S. Zhang, Y. Zhang, B. Yang, J. Hou, *J. Am. Chem. Soc.* **2017**, *139*, 7148.

[13] H. W. Ro, J. M. Downing, S. Engmann, A. A. Herzing, D. M. DeLongchamp, L. J. Richter, S. Mukherjee, H. Ade, M. Abdelsamie, L. K. Jagadamma, A. Amassian, Y. Liu, H. Yan, *Energy Environ. Sci.* **2016**, *9*, 2835.

[14] A. Salleo, R. J. Kline, D. M. DeLongchamp, M. L. Chabinyc, *Adv. Mater.* **2010**, *22*, 3812.

[15] W. Chen, M. P. Nikiforov, S. B. Darling, *Energy Environ. Sci.* **2012**, *5*, 8045.

[16] J. Rivnay, S. C. B. Mannsfeld, C. E. Miller, A. Salleo, M. F. Toney, *Chem. Rev.* **2012**, *112*, 5488.

[17] A. C. Mayer, M. F. Toney, S. R. Scully, J. Rivnay, C. J. Brabec, M. Scharber, M. Koppe, M. Heeney, I. McCulloch, M. D. McGehee, *Adv. Funct. Mater.* **2009**, *19*, 1173.

[18] P. Muller-Buschbaum, *Adv. Mater.* **2014**, *26*, 7692.

[19] L. J. Richter, D. M. Delongchamp, A. Amassian, *Chem. Rev.* **2017**, *117*, 6332.

[20] E. F. Manley, J. Strzalka, T. J. Fauvell, N. E. Jackson, M. J. Leonardi, N. D. Eastham, T. J. Marks, L. X. Chen, *Adv. Mater.* **2017**, *29*, 1703933.

[21] X. Gu, Y. Zhou, K. Gu, T. Kurosawa, Y. Guo, Y. Li, H. Lin, B. C. Schroeder, H. Yan, F. Molina-Lopez, C. J. Tassone, C. Wang, S. C. B. Mannsfeld, H. Yan, D. Zhao, M. F. Toney, Z. Bao, *Adv. Energy Mater.* **2017**, *201602742*, 1.

[22] D. M. Smilgies, R. Li, G. Giri, K. W. Chou, Y. Diao, Z. Bao, A. Amassian, *Phys. Status Solidi - Rapid Res. Lett.* **2013**, *7*, 177.

[23] F. Buss, B. Schmidt-Hansberg, M. Sanyal, C. Munuera, P. Scharfer, W. Schabel, E. Barrena, *Macromolecules* **2016**, *49*, 4867.

[24] N. Shin, L. J. Richter, A. A. Herzing, R. J. Kline, D. M. Delongchamp, *Adv. Energy Mater.* **2013**, *3*, 938.

[25] L. J. Richter, D. M. Delongchamp, F. A. Bokel, S. Engmann, K. W. Chou, A. Amassian, E. Schaible, A. Hexemer, *Adv. Energy Mater.* **2015**, *5*, 1400975.

[26] X. Gu, H. Yan, T. Kurosawa, B. C. Schroeder, K. L. Gu, Y. Zhou, J. W. F. To, S. D. Oosterhout, V. Savikhin, F. Molina-Lopez, C. J. Tassone, S. C. B. Mannsfeld, C. Wang, M. F. Toney, Z. Bao, *Adv. Energy Mater.* **2016**, *6*, 1.

[27] S. Pröller, F. Liu, C. Zhu, C. Wang, T. P. Russell, A. Hexemer, P. Müller-Buschbaum, E. M. Herzig, *Adv. Energy Mater.* **2016**, *6*, 1.

[28] F. Liu, S. Ferdous, E. Schaible, A. Hexemer, M. Church, X. Ding, C. Wang, T. P. Russell, *Adv. Mater.* **2015**, *27*, 886.

[29] R. Li, H. U. Khan, M. M. Payne, D. M. Smilgies, J. E. Anthony, A. Amassian, *Adv. Funct. Mater.* **2013**, *23*, 291.

[30] S. Ebbens, R. Hodgkinson, A. J. Parnell, A. Dunbar, S. J. Martin, P. D. Topham, N. Clarke, J. R. Howse, *ACS Nano* **2011**, *5*, 5124.

[31] K. Zhao, O. Wodo, D. Ren, H. U. Khan, M. R. Niazi, H. Hu, M. Abdelsamie, R. Li, E. Q. Li, L. Yu, B. Yan, M. M. Payne, J. Smith, J. E. Anthony, T. D. Anthopoulos, S. T. Thoroddsen, B. Ganapathysubramanian, A. Amassian, *Adv. Funct. Mater.* **2016**, *26*, 1737.

[32] J. J. van Franeker, M. Turbiez, W. Li, M. M. Wienk, R. a. J. Janssen, *Nat. Commun.* **2015**, *6*, 6229.

[33] M. Abdelsamie, N. D. Treat, K. Zhao, C. McDowell, M. A. Burgers, R. Li, D. M. Smilgies, N. Stingelin, G. C. Bazan, A. Amassian, *Adv. Mater.* **2015**, *27*, 7285.

[34] K. W. Chou, B. Yan, R. Li, E. Q. Li, K. Zhao, D. H. Anjum, S. Alvarez, R. Gassaway, A. Biocca, S. T. Thoroddsen, A. Hexemer, A. Amassian, *Adv. Mater.* **2013**, *25*, 1923.

[35] C. McDowell, M. Abdelsamie, K. Zhao, D.-M. Smilgies, G. C. Bazan, A. Amassian, *Adv. Energy Mater.* **2015**, *5*, 1501121.

[36] L. A. Perez, K. W. Chou, J. A. Love, T. S. van der Poll, D.-M. Smilgies, T.-Q. Nguyen, E. J. Kramer, A. Amassian, G. C. Bazan, *Adv. Mater.* **2013**, *25*, 6380.

[37] K. Wei Chou, H. Ullah Khan, M. R. Niazi, B. Yan, R. Li, M. M. Payne, J. E. Anthony, D.-M. Smilgies, A. Amassian, *J. Mater. Chem. C* **2014**, *2*, 5681.

[38] W. R. Wu, C. J. Su, W. T. Chuang, Y. C. Huang, P. W. Yang, P. C. Lin, C. Y. Chen, T. Y. Yang, A. C. Su, K. H. Wei, C. M. Liu, U. S. Jeng, *Adv. Energy Mater.* **2017**, *7*, 1.

[39] C. M. Hansen, *Hansen Solubility Parameters: A User's Handbook*, CRC Press, Boca Raton, Fl, **2007**.

[40] T. J. Fauvell, T. Zheng, N. E. Jackson, M. A. Ratner, L. Yu, L. X. Chen, *Chem. Mater.* **2016**, *28*, 2814.

[41] S. Ludwigs, *P3HT Revisited – From Molecular Scale to Solar Cell Devices*, Springer, Berlin, **2014**.

[42] L. Lu, L. Yu, *Adv. Mater.* **2014**, *26*, 4413.

[43] T. S. Van Der Poll, J. A. Love, T. Q. Nguyen, G. C. Bazan, *Adv. Mater.* **2012**, *24*, 3646.

[44] B. A. Collins, J. R. Tumbleston, H. Ade, *J. Phys. Chem. Lett.* **2011**, *2*, 3135.

[45] X. Shen, W. Hu, T. P. Russell, *Macromolecules* **2016**, *49*, 4501.

[46] B. A. Collins, Z. Li, J. R. Tumbleston, E. Gann, C. R. Mcneill, H. Ade, *Adv. Energy Mater.* **2013**, *3*, 65.

[47] I. M. Ward, *Structure and Properties of Oriented Polymers*, Springer, **1997**.

[48] J. A. Lim, F. Liu, S. Ferdous, M. Muthukumar, A. L. Briseno, *Mater. Today* **2010**, *13*, 14.

[49] A. A. Y. Guilbert, J. M. Frost, T. Agostinelli, E. Pires, S. Lilliu, J. E. MacDonald, J. Nelson, *Chem. Mater.* **2014**, *26*, 1226.

[50] T. Matsumoto, K. Nishi, S. Tamba, M. Kotera, C. Hongo, A. Mori, T. Nishino, *Polym. (United Kingdom)* **2017**, *119*, 76.

[51] T. S. Van Der Poll, A. Zhugayevych, E. Chertkov, R. C. Bakus, J. E. Coughlin, S. J. Teat, G. C. Bazan, S. Tretiak, *J. Phys. Chem. Lett.* **2014**, *5*, 2700.

[52] J. Liu, B. Walker, A. Tamayo, Y. Zhang, T. Q. Nguyen, *Adv. Funct. Mater.* **2013**, *23*, 47.

[53] N. D. Eisenmenger, G. M. Su, G. C. Welch, C. J. Takacs, G. C. Bazan, E. J. Kramer, M. L. Chabinyc, *Chem. Mater.* **2013**, *25*, 1688.

[54] S. Loser, S. J. Lou, B. M. Savoie, C. J. Bruns, A. Timalsina, M. J. Leonardi, J. Smith, T. Harschneck, R. Turrisi, N. Zhou, C. L. Stern, A. A. Sarjeant, A. Facchetti, R. P. H. Chang, S. I. Stupp, M. A. Ratner, L. X. Chen, T. J. Marks, *J. Mater. Chem. A* **2017**, *5*, 9217.

[55] T. Harschneck, N. Zhou, E. F. Manley, S. J. Lou, X. Yu, M. R. Butler, A. Timalsina, R. Turrisi, M. A. Ratner, L. X. Chen, R. P. H. Chang, A. Facchetti, T. J. Marks, *Chem. Commun.* **2014**, *50*, 4099.

[56] Z. Jiang, X. Li, J. Strzalka, M. Sprung, T. Sun, A. R. Sandy, S. Narayanan, D. R. Lee, J. Wang, *J. Synchrotron Radiat.* **2012**, *19*, 627.

[57] R. Noriega, J. Rivnay, K. Vandewal, F. P. V Koch, N. Stingelin, P. Smith, M. F. Toney, A. Salleo, *Nat. Mater.* **2013**, *12*, 1038.

[58] J. Rivnay, M. F. Toney, Y. Zheng, I. V. Kauvar, Z. Chen, V. Wagner, A. Facchetti, A. Salleo, *Adv. Mater.* **2010**, *22*, 4359.

[59] V. Coropceanu, J. Cornil, D. A. da Silva Filho, Y. Olivier, R. Silbey, J. L. Brédas, *Chem. Rev.* **2007**, *107*, 926.

[60] D. W. Van Krevelen, K. Te Nijenhuis, *Properties of Polymers, Their Correlation with Chemical Structure; Their Numberical Estimation and Prediction From Additive Group Contributions*, Elsevier, Amsterdam, Netherlands, **2009**.

[61] D. Leman, M. A. Kelly, S. Ness, S. Engmann, A. Herzing, C. Snyder, H. W. Ro, R. J. Kline, D. M. DeLongchamp, L. J. Richter, *Macromolecules* **2015**, *48*, 383.

[62] A. F. M. Barton, *CRC Handbook of Solubility Parameters and Other Cohesion Parameters*, CRC Press, **1991**.

[63] K. R. Graham, P. M. Wieruszewski, R. Stalder, M. J. Hartel, J. Mei, F. So, J. R. Reynolds, *Adv. Funct. Mater.* **2012**, *22*, 4801.

[64] J. G. Speight, *The Chemistry and Technology of Petroleum*, CRC Press, **2014**.

[65] S. Zhang, L. Ye, W. Zhao, B. Yang, Q. Wang, J. Hou, *Sci. China Chem.* **2015**, *58*, 248.

[66] H. C. Liao, C. C. Ho, C. Y. Chang, M. H. Jao, S. B. Darling, W. F. Su, *Mater. Today* **2013**, *16*, 326.

[67] G. Reiter, *Chem. Soc. Rev.* **2014**, *43*, 2055.

[68] P. J. Brown, D. S. Thomas, A. Köhler, J. S. Wilson, J.-S. Kim, C. M. Ramsdale, H. Sirringhaus, R. H. Friend, *Phys. Rev. B* **2003**, *67*, 64203.

[69] G. Klaerner, R. D. Miller, *Macromolecules* **1998**, *31*, 2007.

[70] D. Wang, Y. Yuan, Y. Mardiyati, C. Bubeck, K. Koynov, *Macromolecules* **2013**, *46*, 6217.

[71] B. J. Tremolet De Villers, K. A. O'Hara, D. P. Ostrowski, P. H. Biddle, S. E. Shaheen, M. L. Chabinyc, D. C. Olson, N. Kopidakis, *Chem. Mater.* **2016**, *28*, 876.

[72] I. E. Jacobs, F. Wang, Z. I. Bedolla Valdez, A. N. Ayala Oviedo, D. J. Bilsky, A. J. Moulé, *J. Mater. Chem. C* **2018**, *6*, DOI 10.1039/C7TC04358A.

[73] P. Vanlaeke, A. Swinnen, I. Haeldermans, G. Vanhoyland, T. Aernouts, D. Cheyns, C. Deibel, J. D'Haen, P. Heremans, J. Poortmans, J. V. Manca, *Sol. Energy Mater. Sol. Cells* **2006**, *90*, 2150.

[74] S. S. Van Bavel, M. Bärenklau, G. De With, H. Hoppe, J. Loos, *Adv. Funct. Mater.* **2010**, *20*, 1458.

[75] C. H. Woo, C. Piliego, T. W. Holcombe, M. F. Toney, J. M. J. Fréchet, *Macromolecules* **2012**, *45*, 3057.

[76] P. E. Hopkinson, P. A. Staniec, A. J. Pearson, A. D. F. Dunbar, T. Wang, A. J. Ryan, R. A. L. Jones, D. G. Lidzey, A. M. Donald, *Macromolecules* **2011**, *44*, 2908.

[77] D. M. González, C. J. Schaffer, S. Pröller, J. Schlipf, L. Song, S. Bernstorff, E. M. Herzig, P. Müller-Buschbaum, *ACS Appl. Mater. Interfaces* **2017**, *9*, 3282.

[78] N. Kleinhenz, N. Persson, Z. Xue, P. H. Chu, G. Wang, Z. Yuan, M. A. McBride, D. Choi, M. A. Grover, E. Reichmanis, *Chem. Mater.* **2016**, *28*, 3905.

[79] F. Liu, W. Zhao, J. R. Tumbleston, C. Wang, Y. Gu, D. Wang, A. L. Briseno, H. Ade, T. P. Russell, *Adv. Energy Mater.* **2014**, *4*, 1.

[80] N. Zhou, H. Lin, S. J. Lou, X. Yu, P. Guo, E. F. Manley, S. Loser, P. Hartnett, H. Huang, M. R. Wasielewski, L. X. Chen, R. P. H. Chang, A. Facchetti, T. J. Marks, *Adv. Energy Mater.* **2014**, *4*, 1300785.

[81] M. R. Hammond, R. J. Kline, A. A. Herzing, L. J. Richter, D. S. Germack, H. W. Ro, C. L. Soles, D. A. Fischer, T. Xu, L. Yu, M. F. Toney, D. M. Delongchamp, *ACS Nano* **2011**, *5*, 8248.

[82] J. M. Szarko, J. Guo, Y. Liang, B. Lee, B. S. Rolczynski, J. Strzalka, T. Xu, S. Loser, T. J. Marks, L. Yu, L. X. Chen, *Adv. Mater.* **2010**, *22*, 5468.

[83] Y. J. Kim, D. S. Chung, C. E. Park, *Nano Energy* **2015**, *15*, 343.

[84] A. K. Ko Kyaw, D. Gehrig, J. Zhang, Y. Huang, G. C. Bazan, F. Laquai, T.-Q. Nguyen, *J. Mater. Chem. A* **2015**, *3*, 1530.

[85] Y. Huang, W. Wen, S. Mukherjee, H. Ade, E. J. Kramer, G. C. Bazan, *Adv. Mater.* **2014**, *26*, 4168.

[86] A. K. K. Kyaw, D. H. Wang, C. Luo, Y. Cao, T.-Q. Nguyen, G. C. Bazan, A. J. Heeger, *Adv. Energy Mater.* **2014**, *4*, 1301469.

[87] J. A. Love, C. M. Proctor, J. Liu, C. J. Takacs, A. Sharenko, T. S. Van Der Poll, A. J. Heeger, G. C. Bazan, T. Q. Nguyen, *Adv. Funct. Mater.* **2013**, *23*, 5019.

[88] N. A. Ran, S. Roland, J. A. Love, V. Savikhin, C. J. Takacs, Y. T. Fu, H. Li, V. Coropceanu, X. Liu, J. L. Brédas, G. C. Bazan, M. F. Toney, Di. Neher, T. Q. Nguyen, *Nat. Commun.* **2017**, *8*, 1.

[89] K. J. Fallon, N. Wijeyasinghe, E. F. Manley, S. D. Dimitrov, S. A. Yousaf, R. S. Ashraf, W. Duffy, A. A. Y. Guilbert, D. M. E. Freeman, M. Al-Hashimi, J. Nelson, J. R. Durrant, L. X. Chen, I. McCulloch, T. J. Marks, T. M. Clarke, T. D. Anthopoulos, H. Bronstein, *Chem. Mater.* **2016**, *28*, 8366.

[90] S. Wang, S. Fabiano, S. Himmelberger, S. Puzinas, X. Crispin, A. Salleo, M. Berggren, *Proc. Natl. Acad. Sci.* **2015**, *112*, 10599.

[91] J. A. Love, S. D. Collins, I. Nagao, S. Mukherjee, H. Ade, G. C. Bazan, T. Q. Nguyen, *Adv. Mater.* **2014**, *26*, 7308.

Figures

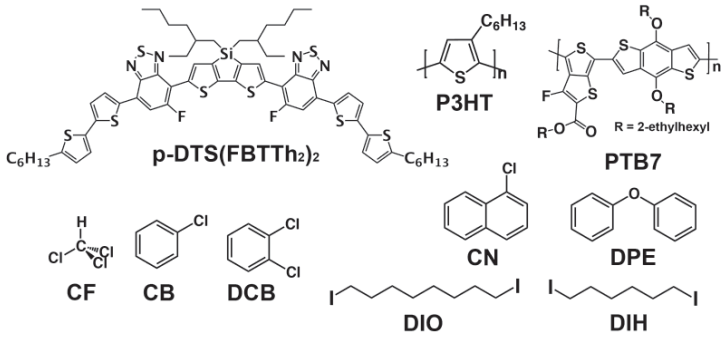

Figure 1. Molecular structures of the organic semiconductors (top), solvents (bottom left), and additives (bottom right) studied in this work. For brevity, p-DTS(FBTTH$_2$)$_2$ is named **DTS** in the text. Full chemical names are given in the Introduction.

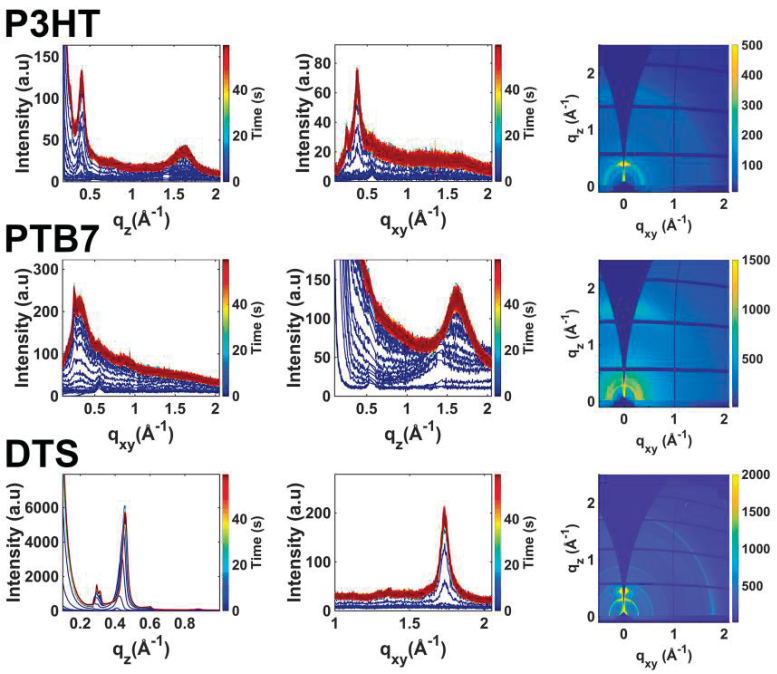

Figure 2. GIWAXS-derived crystallization for all three indicated semiconductors spun from CF solutions. Lamellar (left) and π-π stacking (middle) evolutions are both shown. Each line cut represents a 100 ms time point, the entire spin-coating period is shown. Post-processing 2D scattering images of the final finished evolution are shown on the right.

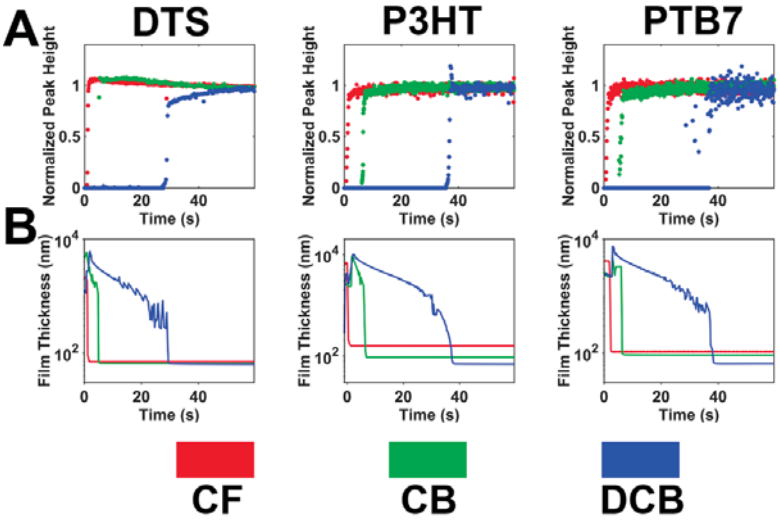

Figure 3. (A) Normalized evolution of the fitted GIWAXS peak heights for the lamellar (100) reflections of the indicated semiconductors and (B) Time dependence of film thickness as measured by in situ optical reflectance during the x-ray measurement for all additive-free single solvent films.

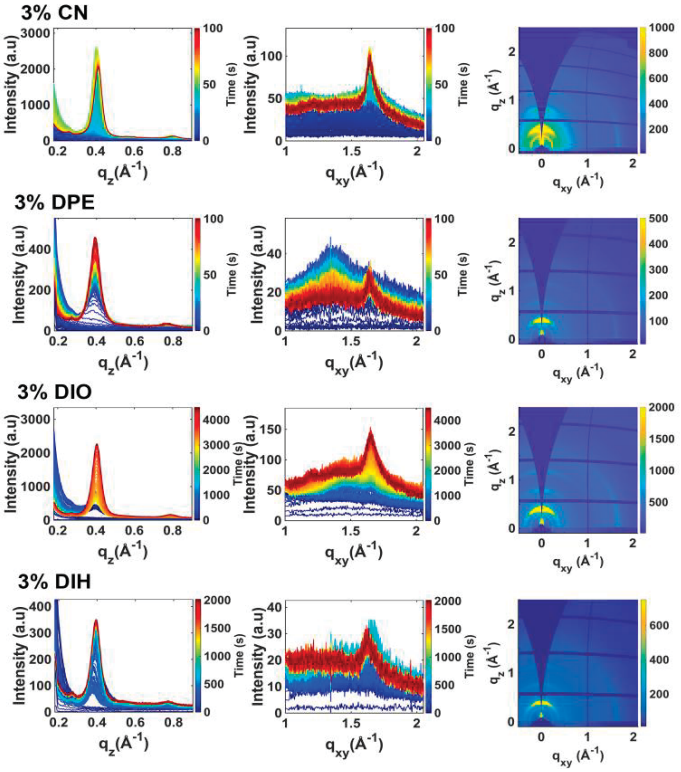

Figure 4. GIWAXS-derived crystalline growth for **P3HT** films spun from the indicated 3% v/v additive solutions in CB. Lamellar (left) and π-π stacking (middle) evolutions are both shown. The post-processing 2D scattering images of the final complete evolution are shown on the right.

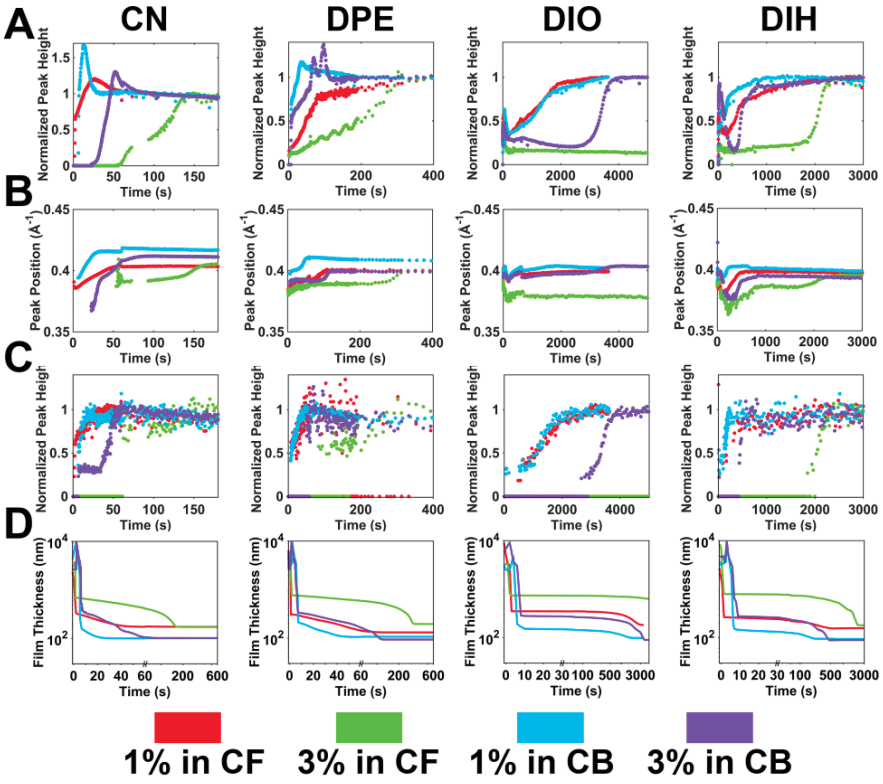

Figure 5. Fitted peak temporal evolution of **P3HT** (100) lamellar and (010) π-π stacking reflections for all additive processed **P3HT** films with (A) normalized evolution of the (100) lamellar fitted peak height; (B) evolution of the (100) lamellar fitted peak position; and (C) normalized evolution of the (010) π-π stacking fitted peak height. (D) Time-dependent film thickness as measured by *in situ* optical reflectance during the x-ray measurements.

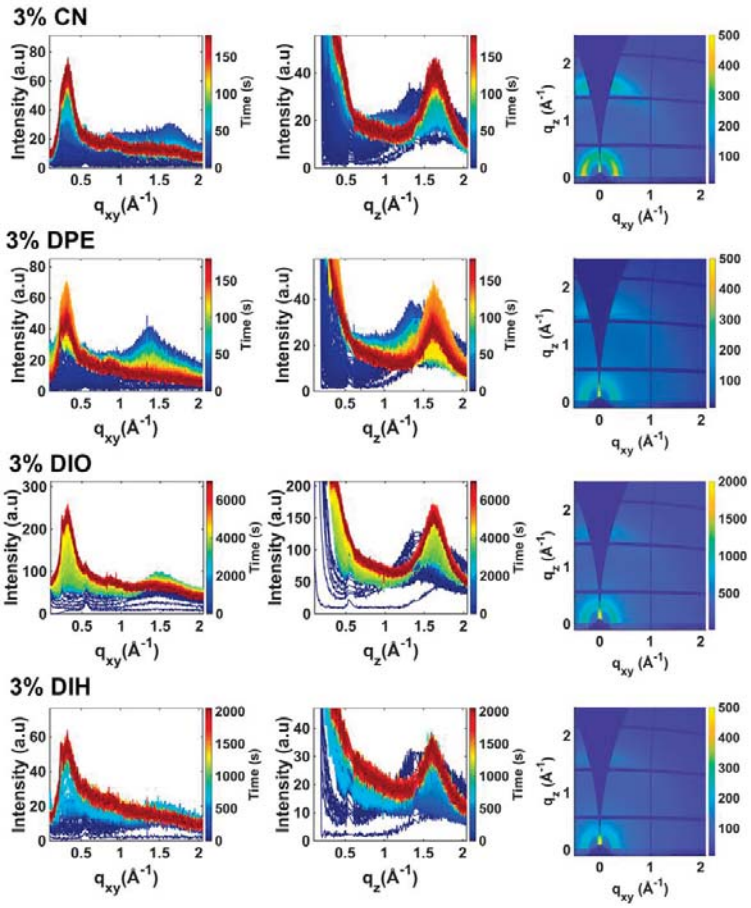

Figure 6. GIWAXS-derived crystallization data for **PTB7** films spun from 3% v/v additive solutions in CB. Lamellar (left) and π-π stacking (middle) evolutions are both shown. Post-processing 2D scattering images of the final scattering patterns are shown on the right.

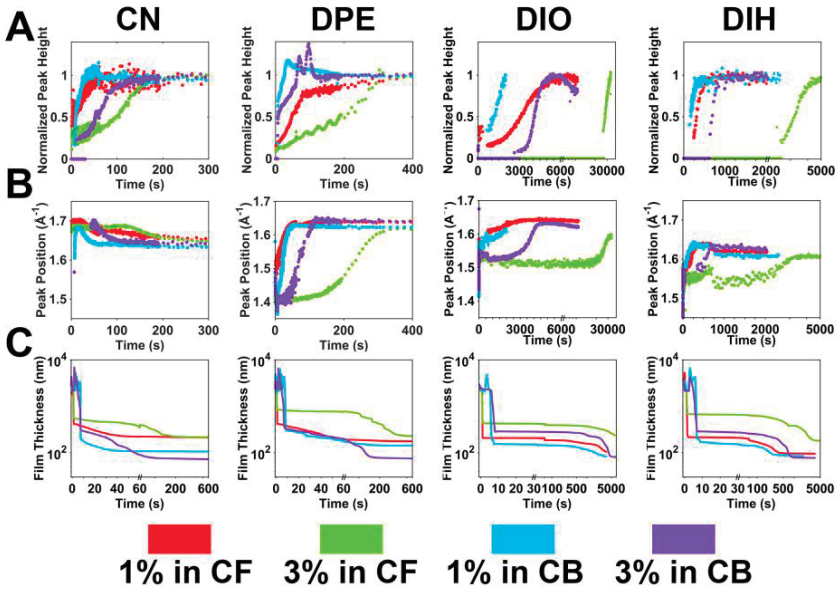

Figure 7. Fitted peak evolution of **PTB7** (100) lamellar and (010) π-π stacking reflections for all additive-processed **PTB7** films with, (A) Normalized evolution of the (100) lamellar fitted

peak height, (B) Peak position evolution of the out-of-plane scattering feature as it transitions from additive scattering to (010) π-π stacking scattering, and (C) Time dependence of film thickness measured in parallel by *in situ* optical reflectance. Note that a sharp change in thickness occurs for some samples at 60 s due to the end of spinning and anisotropic coating of the substrate.

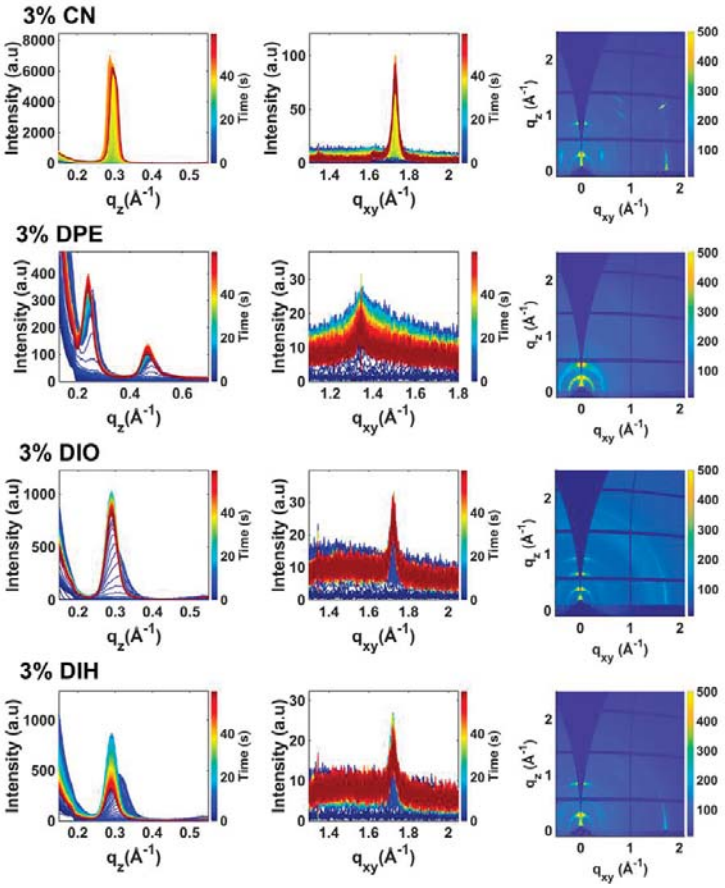

Figure 8. GIWAXS derived crystallization data for **DTS** films spun from CB solutions with the indicated 3% v/v of the indicated additives. Lamellar (left) and π-π stacking (middle) evolutions are both shown.

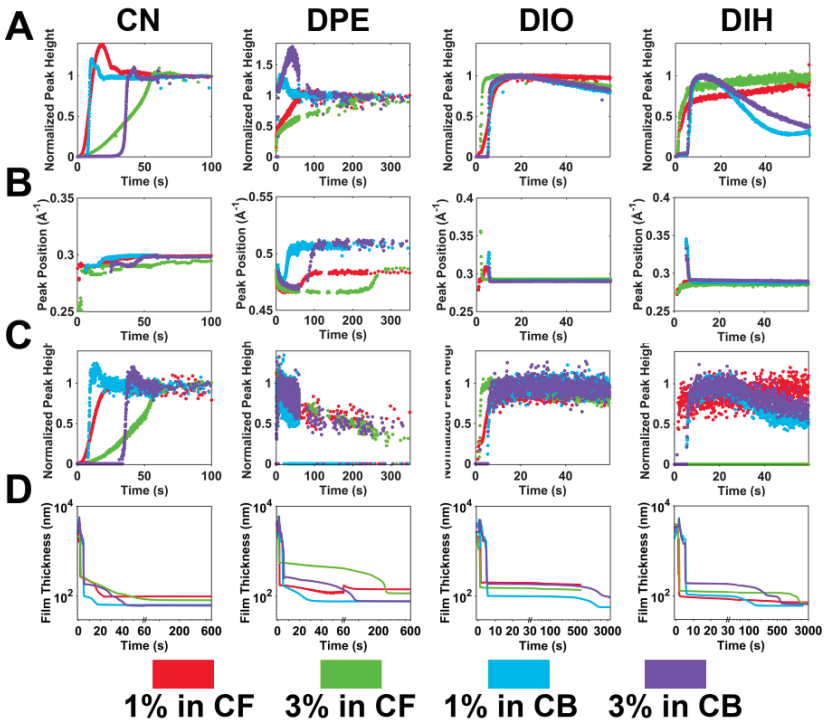

Figure 9. Fitted GIWAXS peak evolution of **DTS** side-chain stacking and π-π stacking peaks for the indicated additive-processed **DTS** films with (A) Normalized evolution of the side chain stacking fitted peak height; (B) Evolution of the side chain stacking fitted peak position; and (C) Normalized evolution of the π-π stacking fitted peak height, and (D) Film thickness over time as measured by *in situ* optical reflectance during the GIWAXS measurement. Note, DPE-processed film peak height and position data are taken from the n = 2 peak due to overlap of the n = 1 peak with the exponential scattering decay background. Also note an abrupt change in thickness occurs for some samples at 60 s due to the end of spinning and anisotropic coating of the substrate.

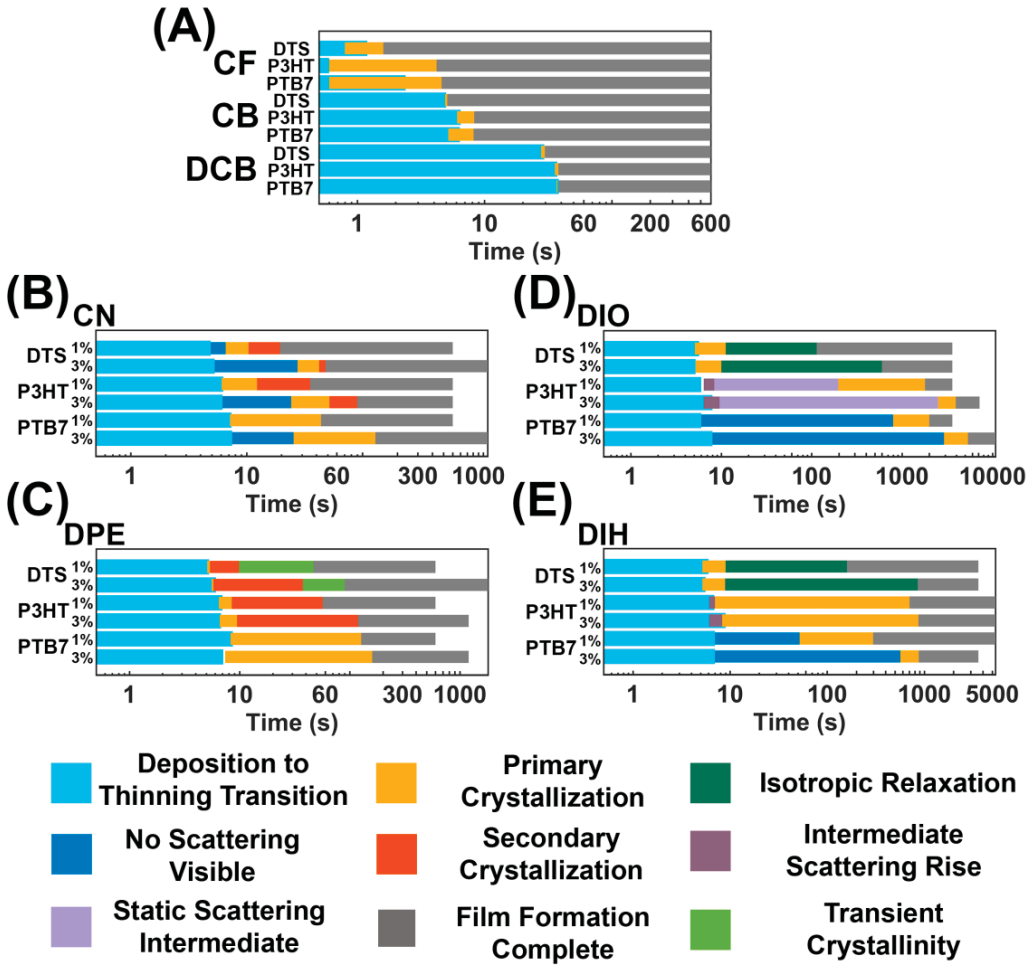

Figure 10. Morphology evolution summary for all single-solvent and all additive containing CB films. Films are sorted by additive to easily compare evolution across different semiconductors. Different phases of formation are labeled; grey areas indicate that no further evolution is detected.

Tables

Table 1. Summary of morphology formation data for single-solvent processed **P3HT**, **DTS**, and **PTB7** films.

	Solvent	t_{thin} (s)	Crystallization Onset (s)	Crystallization Complete (s)
P3HT	**CF**	0.6	0.6	4.2
	CB	6.5	6.1	8.3
	DCB	37.3	35.8	38
PTB7	**CF**	2.4	0.6	4.6
	CB	6.4	5.2	8.2
	DCB	38.3	36.8	37.4
DTS	**CF**	1.2	0.8	1.6
	CB	5.0	4.9	5.1
	DCB	29.5	27.9	29.8

Table 2. Summary of morphology formation data for P3HT films processed with additives in CF and CB. The secondary and tertiary crystallization steps differ depending on the additive used and are labeled with a superscript indicating the specific type of crystallization process the time points indicate.

P3HT		**Thickness Evolution**		**Crystallization**			
Solvent/Additive		t_{thin} (s)	t_{finish} (s)	**Onset (s)**	**Crystallization Step 2 (s)**	**Crystallization Step 3 (s)**	**Complete (s)**
CN	**1% v/v in CF**	2	61	1.2	59 [a]	-	26.1
	3% v/v in CF	1.4	170	55.4	93.4 [a]	-	140.9
	1% v/v in CB	6.3	26	6.1	12.3 [a]	-	35.4
	3% v/v in CB	6.2	77	24.2	51.9 [a]	-	90
DPE	**1% v/v in CF**	1	98	1.2	2 [b]	-	110
	3% v/v in CF	1.6	328	1.1	1.5 [b]	-	332
	1% v/v in CB	7	46	6.5	8.5 [b]	-	56.8
	3% v/v in CB	6.8	116	6.6	9.5 [b]	-	119
DIO	**1% v/v in CF**	2	3137	1.3[*]	3.5 [c]	194 [d]	1918
	3% v/v in CF[#]	3	-	1[*]	3 [c]	--	--
	1% v/v in CB	6	1738	6.4[*]	8.4 [c]	197 [d]	1800
	3% v/v in CB	8	3848	6.4[*]	9.6 [c]	2500 [d]	3929
DIH	**1% v/v in CF**	1.5	449	1	2.2 [c]	-	620
	3% v/v in CF	1.5	2209	1	2.5 [c]	-	2630
	1% v/v in CB	6.9	208	6.1	7 [c]	-	705
	3% v/v in CB	9	462	6.1	8.3 [c]	-	870

[a)]Secondary Evolution Start; [b)] Oscillatory Peak Growth; [c)] Intermediate Formed; [d)]Primary Crystallization Starts; [*)] Intermediate Onset; [#)] Primary crystal growth did not occur within 5 hr observation window.

Table 3. Summary of morphology formation data for **PTB7** films processed with additives in CF and CB.

PTB7		Thickness Evolution		Crystallization	
Solvent/Additive		**t_{thin} (s)**	**t_{finish} (s)**	**Onset (s)**	**Complete (s)**
CN	**1% v/v in CF**	2	61	1.4	55.4
	3% v/v in CF	1.4	170	1.3	177
	1% v/v in CB	6.3	26	7.2	43.8
	3% v/v in CB	6.2	77	25.4	129
DPE	**1% v/v in CF**	1	250	1.5	51.4
	3% v/v in CF	0.8	451	1.7	336
	1% v/v in CB	8.7	217	8.3	127
	3% v/v in CB	7.1	383	7.4	160
DIO	**1% v/v in CF**	1	-*	677	6070
	3% v/v in CF	1	-*	26860	33460
	1% v/v in CB	6	3351	795	2000
	3% v/v in CB	8	5844	2914	5354
DIH	**1% v/v in CF**	1.5	535	181	837
	3% v/v in CF	1.5	4094	2095	4626
	1% v/v in CB	7	393	52	297
	3% v/v in CB	7	1035	565	877

*) Due to reduced observation times in the reflectance measurements in comparison to the x-ray measurements t_{finish} times could not be recorded for the CF:DIO-processed films.

Table 4. Summary of morphology formation data for **DTS** films processed with the indicated additives in CF and CB. The secondary and tertiary crystallization steps differ depending on the additive used and are labeled with a superscript indicating the specific type of crystallization process the time points indicate.

DTS		Thickness Evolution		Crystallization			
Solvent/Additive		t_{thin} (s)	t_{finish} (s)	Onset (s)	Crystallization step 2 (s)	Crystallization step 3 (s)	Complete (s)
CN	1% v/v in CF	1.6	26	1.1	-	-	32.5
	3% v/v in CF	2.2	100	3.5	-	-	57.6
	1% v/v in CB	4.9	23	6.6	10.4[a]	-	19.5
	3% v/v in CB	5.3	47	27.5	42.24[a]	-	48
DPE	1% v/v in CF	1.8	141	1	1.3[a]	250[c]	292
	3% v/v in CF	1.4	340	1	1.3[a]		64
	1% v/v in CB	5.3	41	5.1	5.4[a]	9.9[c]	47
	3% v/v in CB	6.1	114	5.6	5.8[a]	37.5[c]	90
DIO	1% v/v in CF	1.6	-	1.1	13.3[b]	-	205*
	3% v/v in CF[#]	1.2	-	1.8	4.6[b]	-	181*
	1% v/v in CB	5.7	1900	5.1	11.2[b]	-	114*
	3% v/v in CB	5.2	3657	5.2	10[b]	-	600*
DIH	1% v/v in CF	1.8	672	1	5.3[b]	-	773*
	3% v/v in CF	2	2247	1	5.5[b]	-	2158*
	1% v/v in CB	6	180	5.2	9[b]	-	160*
	3% v/v in CB	5.6	895	5.2	8.9[b]	-	856*

[a)]Secondary Evolution Start; [b)] Primary Crystallization Complete; [c)] Transient Peak Height Start; *) 'Isotropic Relaxation' Complete.

Table 5. Summary of interaction radii (Ra) for the indicated processing additives with the indicated semiconductors calculated using Hansen solubility parameters and the group contribution method.[60–63] Full calculation details for all parameters are available in the SI. EHO denotes ethylhexyloxy **PTB7** sidechains while hexyl denotes **P3HT** sidechains.

Additive	DIO R_a ($MPa^{1/2}$)	DIH R_a ($MPa^{1/2}$)	CN R_a ($MPa^{1/2}$)	DPE R_a ($MPa^{1/2}$)
PTB7	9.9	9.6	6.2	5.7
P3HT	2.0	2.2	3.4	2.8
DTS	7.4	7.1	6.9	3.6
EHO	2.7	3.8	6.7	5.9
Hexyl	7.9	9.0	10.5	10.7

A detailed in situ GIWAXS analysis of the spin-coating of P3HT, PTB7 and p-DTS(FBTTS)$_2$ organic photovoltaic films reveals dramatic changes in morphological evolution that occur depending on the solvent and additives used in the processing. This work identifies key impacts caused by the difference between kinetically and thermodynamically driven morphologies as well as the specific molecular interactions between semiconducting materials and additive molecules. Guidelines are provided for solvent and additive choice based on desired morphological properties.

Keyword: in situ GIWAXS, spin-coating, additive, polymer, organic solar cells

Eric F. Manley, Joseph Strzalka, Thomas J. Fauvell, Tobin J. Marks*, Lin X. Chen*

Solvent and Additive Effects on Film Formation Dynamics for Spin-Cast Small-Molecule and Polymer Solar Cell Materials

ToC figure ((Please choose one size: 55 mm broad × 50 mm high **or** 110 mm broad × 20 mm high. Please do not use any other dimensions))